Composite Structures 345 (2024) 118276

Contents lists available at ScienceDirect

Composite Structures

journal homepage: www.elsevier.com/locate/compstruct

Non-linear buckling analysis of delaminated hat-stringer panels using variational asymptotic method

A. Phanendra Kumar [a], Javier Paz Méndez [b,c], Ramesh Gupta Burela [e], Chiara Bisagni [b,d], Dineshkumar Harursampath [a], Sathiskumar Anusuya Ponnusami [f,*]

[a] NMCAD Laboratory, Department of Aerospace Engineering, Indian Institute of Science, Bengaluru, Karnataka, India
[b] Faculty of Aerospace Engineering, Delft University of Technology, Delft, The Netherlands
[c] Universidad Rey Juan Carlos - Aerospace Systems and Transport Research Group, Madrid, Spain
[d] Department of Aerospace Science and Technology, Politecnico di Milano, Milano, Italy
[e] Department of Civil Engineering, National Institute of Technical Teachers' Training and Research, Bhopal, India
[f] Department of Engineering, City, University of London, London, United Kingdom

ARTICLE INFO

Keywords:
Non-linear buckling
Hat-stringer panel
Delamination
3-D finite element analysis
Variational asymptotic method
Stiffened composite structure

ABSTRACT

This research proposes a computationally efficient methodology using a Constrained Variational Asymptotic Method (C-VAM) for non-linear buckling analysis on a hat-stringer panel with delamination defects. Starting with the geometrically non-linear kinematics, the VAM procedure reduces the three-dimensional (3-D) strain energy functional to an analogous 2-D plate model and evaluates the closed form warping solutions. Utilising the resulting warping solutions and recovery relations for the skin and the stringer, displacement continuity at the three-dimensional level is enforced between the stringer and the skin based on the pristine and delaminated interface regions. Consequently, the constrained matrices obtained from C-VAM is incorporated into an in-house developed non-linear finite element framework. Using the developed formulation, a stiffened panel with delamination of 40 mm between the stringer and the skin is analysed under compression. The results have been validated locally and globally, employing experimental data and 3-D finite element analysis (FEA). Experiments are carried out on the co-cured panel by applying quasi-static loading with displacement-controlled conditions, and 3-D FEA is carried out in Abaqus. Load-response plots have been obtained to validate the results at the global level, and they are in excellent agreement with experiments and 3-D FEA. Subsequently, out-of-plane displacement contour plots are obtained; the number of half waves and wave intensity in 3-D FEA and C-VAM are comparable, although there are minor differences compared to the experimental findings. The proposed framework is shown to be computationally efficient by over 55% as compared to 3-D FEA for performing non-linear buckling analysis on the stiffened composite structure considered in the current work.

1. Introduction

Composite structures have revolutionised the field of engineering, offering exceptional mechanical properties and weight-saving advantages [1]. Among various classes of composite structures, stiffened panels have attracted considerable attention due to their superior load-carrying capacity and structural efficiency [2,3]. The aerospace industry extensively uses hat-stringer panels to design aircraft structures such as fuselage sections, wing skins, and stabilisers. Understanding the behaviour of hat-stringer panels, especially their buckling response, is crucial for the design, optimisation, and structural integrity assessment of composite structures. The buckling behaviour of stiffened panels is more complex than a non-stiffened composite structure and influenced by multiple factors such as geometric configurations, material properties, load conditions, and the presence of delaminations [4]. Despite their numerous advantages, hat-stringer panels are susceptible to delaminations, which are interfacial failures between the skin and the stringer [5]. Such delaminations occur due to manufacturing defects, impact events, fatigue, or exposure to environmental conditions [6]. These defects, in turn, act as stress concentrators, reducing the effective load-carrying capacity and stiffness of the panels and can lead to catastrophic failure if not adequately addressed. Therefore, a comprehensive understanding of delaminated hat-stringer panels under buckling is crucial for ensuring composite structure's structural integrity and reliability in practical engineering applications.

To comprehend the behaviour of stiffened composite panels under buckling, various methods have been developed, including analytical,

* Corresponding author.
E-mail address: sathiskumar.ponnusami@city.ac.uk (S.A. Ponnusami).

https://doi.org/10.1016/j.compstruct.2024.118276
Received 30 November 2023; Received in revised form 12 May 2024; Accepted 11 June 2024
Available online 4 July 2024

numerical, and experimental approaches [7–15]. Zhou et al. [16] evaluated the buckling modes of stiffened panels subjected only to pure bending by developing an analytical solution based on the equilibrium approach. In this approach, it is assumed that both the stiffener and the plate will follow the Kirchhoff–Love plate theory (displacement kinematics are assumed apriori). Huang and Qiao [17] proposed a semi-analytical method to evaluate the buckling modes of the stiffened panel under compression loads. In this method, characteristic equations using the governing equation of the plate with stiffeners along two orthogonal directions are solved using the Galerkin method. Based on the position of the stiffeners in the plate, the stiffened plate is modelled as a plate with varying stiffness. Even in this formulation, the assumptions from the classical plate theory are considered. These methods rely on simplifying assumptions and may not accurately capture the complex behaviour of delaminated hat-stringer panels. However, they provide valuable insights into the dominant buckling modes of stiffened panels. In most of the existing methods, either asymptotic or variational principle-based methods, engineering structures are analysed by formulating potential energy functional (PEF) [18]. Both these methods have their own advantages and disadvantages. Variation asymptotic formulation exploits the advantages of the asymptotic and variational methods. The existing methodologies proposed in the literature for analysing these stiffened structures are either considered as a single component instead of taking the stiffener and plate as separate components or if the constraints are being incorporated between stiffener and plate, those continuity conditions are being implemented at a 2-D level only [19]. These methods cannot accurately provide the deformation behaviour; they will either underestimate or overestimate it [20]. As the name suggests, the current proposed C-VAM formulation combines variational and asymptotic approaches, constraining the stiffener and plate at the 3-D level but not at the 2-D level, exploiting the advantages of the asymptotic and variational methods [18]. The strength of the current C-VAM and its novelty is that it can analyse structures with multiple components and interface delaminations.

Numerical methods, such as FEA, offer an efficient tool for detailed buckling analysis of composite structures [21–25]. FEA provides accurate results but requires significant computational resources and time for detailed analysis. Experimental methods involve conducting physical tests on down-scale or full-scale models to evaluate the buckling characteristics of stiffened panels [7,9,10,26–30]. These tests provide valuable data for the validation of numerical models and offer insights into the real-world behaviour of composite structures. Experimental tests are essential for understanding the failure mechanisms and validating numerical models [31–33].

While modelling using FEA is proven to be reliable, the computational time shoots up when it comes to three-dimensional non-linear buckling analysis of complex composite structures such as stiffened panels. In this context, we have employed the variational asymptotic method (VAM) to derive reduced-order non-linear plate models for the stringer and skin. These two components are integrated as a stiffened structure by enforcing interface continuity (or discontinuity in the presence of delamination) using the recovered 3-D displacement fields.

Unlike the existing dimensionally-reduced plate/shell models, VAM starts with attaining 2-D equivalent energy functional integrating the 3-D strain energy functional across the thickness of the plate for dimensional reduction [34–39]. Using the small parameters existing in the problems, such as the thickness-to-length ratio in the case of plates/shells, the energy is expressed in terms of these small parameters using order analysis and is asymptotically reduced, followed by minimisation using variational principles. The resulting Euler–Lagrange equations from the variational statement are solved to obtain the unknown warping fields in the thickness face in the case of plates/shells [40]. Upon substituting back into the 3-D energy functional, these warping fields provide the 2-D equivalent plate/shell energy and the associated plate/shell constitutive law or the stiffness matrix. The original idea of the authors lies in evaluating the influence of delamination in composite structures on the nonlinear buckling behaviour, which is relevant in analysing aerospace structures. The proposed nonlinear framework can readily be extended to analyse complex multicomponent structures with multiple delaminations. In conventional VAM analysis or any existing dimensionally reduced formulations, the continuity is ensured at the dimensionally reduced 2-D level (2-D continuity) but not at the 3-D level. This 2-D continuity cannot accurately capture the delaminated structure's deformation behaviour. The detailed mathematical description of the constraint VAM (C-VAM) formulation used to analyse the hat-stringer panel is given in Section 2. The advantage of the proposed VAM formulation lies in its ability to handle complex composite structures, including delaminations, while significantly reducing computational effort compared to FEA. Apart from computational efficiency, the advantage is that the current C-VAM methodology provides closed-formed warping solutions. Using the proposed framework, optimisation studies can be performed using C-VAM, where the objective is to attain the geometric configuration for the structure with minimal warpings and eventually improved buckling behaviour. One application among many others where this particular optimisation study can be proven advantageous is wind turbine blades. By ensuring minimal warpings, we can ensure that the blades maintain their aerodynamic profile, resulting in efficient energy storage. One of the main limitations of the current methodology is that it applies to only thin structures. Further, while the framework models the presence of static delamination, the damage evolution modelling has not been incorporated into the method currently; therefore, once the delamination starts propagating from one side of the foot of the stringer to the other side, the deformation behaviour of the stiffened panel cannot be accurately evaluated.

In the above context, this paper comprehensively examines the delaminated hat-stringer panel's non-linear buckling characteristics using the C-VAM. C-VAM analysis results are verified with 3-D FEA and validated with experimental results to affirm the usage of the suggested methodology. The accuracy and efficiency of C-VAM in predicting the buckling behaviour of delaminated hat-stringer panels is demonstrated, highlighting its potential as a valuable tool for designing stiffened panels with complex stiffener configurations.

This article has five sections, where Section 2 focuses on the C-VAM formulation employed in analysing the buckling characteristics of the stiffened panels with delaminations. The experimental details of compression testing of the hat-stringer panel and detailed 3-D finite element analysis are presented in Section 3. Validation of the presented methodology and results of non-linear buckling analysis obtained from all three analyses (C-VAM, 3-D FEA and experiments) are explained and compared in Section 4. Finally, conclusions from the current study are mentioned in Section 5.

2. Constraint VAM (C-VAM) formulation

This section describes the formulation and implementation of the stiffened plate model using C-VAM. It starts with the plate kinematics and the 2-D constitutive law evaluation from the 3-D strain energies of the hat-stringer and plate of the stiffened panel, which is shown in Fig. 1. The gold colour area in the figure represents the delamination between the feet of the stringer and the plate in the stiffened panel. This is followed by the constraint VAM formulation and implementation details specific to the hat-stringer panel with existing delamination defects.

2.1. Three-dimensional plate kinematics

The kinematics mentioned in this subsection are formulated by Hodges et al. [41]. In this formulation, the mid-plate surface is deemed the reference surface due to the smaller plate thickness than the other two dimensions. Unless otherwise specified, all Greek indices (α and β)

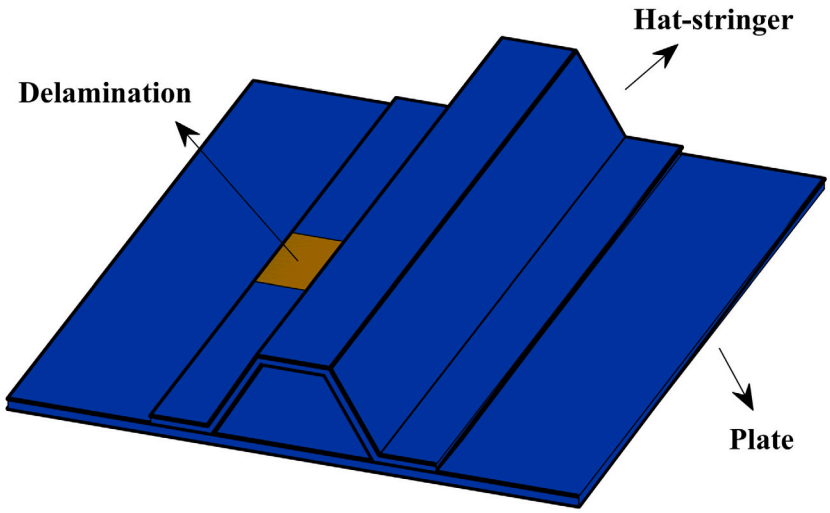

Fig. 1. Hat-stringer panel with static delamination, which is highlighted in gold.

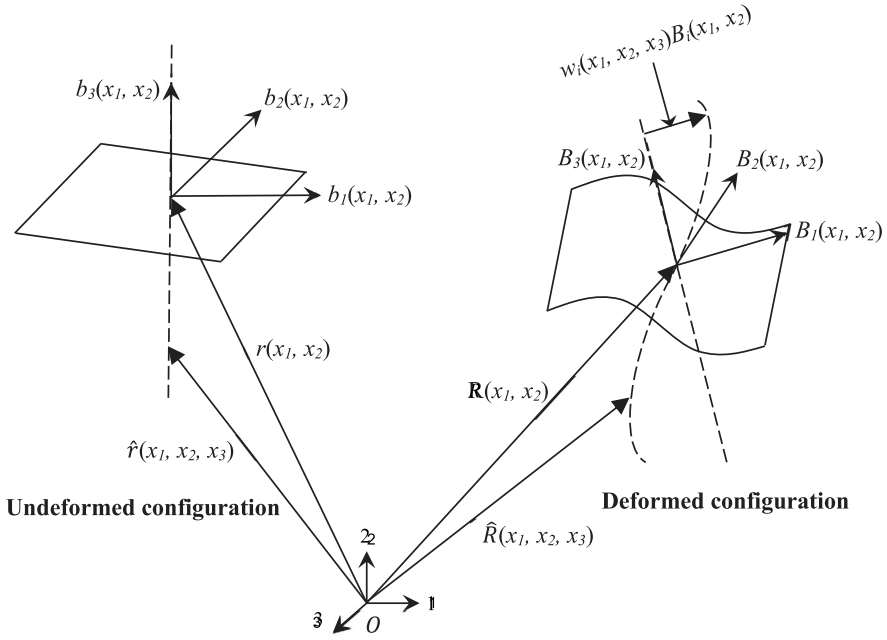

Fig. 2. Schematic of the plate's deformed and undeformed reference configurations with kinematics parameters.

are assigned the values 1 and 2, and all Latin indices (i, j and k) are assigned the values 1, 2, and 3. Reference surfaces with undeformed and deformed configurations, along with the different kinematic parameters involved in the current formulation, are shown in Fig. 2.

The coordinates (x_1, x_2) represent the material points on both the configurations as shown in Fig. 2. x_3 denotes points distant from the reference surfaces. The orthonormal unit basis vectors in the undeformed and deformed configurations along x_i are denoted as b_i and B_i, respectively. The orthogonal basis vectors are related to one another using the directional cosine matrix $C(x_1, x_2)$ as shown in Eq. (1).

$$B_i(x_1, x_2) = C_{ij}(x_1, x_2) b_j(x_1, x_2) \tag{1}$$

Position vectors in both the configurations are denoted using $r(x_1, x_2)$ and $R(x_1, x_2)$. The Eq. (2) gives any position on the undeformed configuration. The applied load on the undeformed stiffened panel configuration results in the deformed configuration of the panel, including the warpings $w_i(x_1, x_2, x_3)$ in the ith direction. Eq. (3) shows the position vector in the deformed configuration.

$$\hat{r}(x_1, x_2, x_3) = r(x_1, x_2) + x_3 b_3(x_1, x_2) \tag{2}$$

$$\hat{R}(x_1, x_2, x_3) = R(x_1, x_2) + x_3 B_3(x_1, x_2) + w_i(x_1, x_2, x_3) B_i(x_1, x_2) \tag{3}$$

Non-linear strain components (Γ_{ij}) resulting from the applied compressive load are obtained using Eq. (4), which depends on the deformation gradient components.

$$\Gamma_{ij} = \frac{1}{2}(F_{ik}F_{kj} - I_{ij}) \tag{4}$$

Where the deformation gradient tensor denoted as F_{ij} is obtained by using contravariant (g^j) base vectors of undeformed and covariant (G_i) base vectors of deformed configurations ($F_{ij} = G_i g^j$) and I_{ij} is the identity matrix. Covariant-based vectors are the tangential base vectors for the configurations and can be obtained using Eq. (5) and Eq. (6).

$$g_i = \frac{\partial \hat{r}}{\partial x_i} \tag{5}$$

$$G_i = \frac{\partial \hat{R}}{\partial x_i} \tag{6}$$

The undeformed configuration has contravariant basis vectors obtained using Eq. (7), perpendicular to the reference surfaces.

$$g^j = \frac{1}{2\sqrt{g}} e_{jki}(g_k \times g_i) \tag{7}$$

Obtaining these covariant and contravariant base vectors involves the evaluation of the derivative of the position vector ($\hat{R}$) and base vectors (B_i) called 2-D generalised strain measures ($B_{i,\alpha}$, $R_{,\alpha}$), which are analogous to those proposed by Reissner [42]. The 2-D generalised strain measures are given in Eq. (8).

$$R_{,\alpha} = B_\alpha + 2\gamma_{\alpha 3} B_3 + \epsilon_{\alpha\beta} B_\beta \qquad B_{i,\alpha} = (K_{\alpha 3} B_3 - K_{\alpha\beta}(B_\beta \times B_3)) \times B_i \tag{8}$$

Where $\gamma_{\alpha 3}$ and $K_{\alpha 3}$ are 2-D transverse strain and curvature respectively. $\epsilon_{\alpha\beta}$ and $K_{\alpha\beta}$ are 2-D in-plane strain and curvature measures respectively.

2.2. Potential energy functional

In this subsection, potential energy functional (Π^*) is formulated using the potential energy (Π) and the warping constraints.

2.2.1. Potential energy

We can obtain the potential energy in terms of work done (W) and strain energy (U) for the three-dimensional geometrical non-linear analysis. Total strain energy is the summation of the strain energies of all the individual lamina in the laminate in terms of the constitutive matrix ($\boldsymbol{C}$) of the lamina and 3-D strains ($\boldsymbol{\Gamma}$) as given in Eq. (9). The angular brackets $\langle\,\rangle$ represent the integration across the laminate's thickness.

$$U = \frac{1}{2}\langle \boldsymbol{\Gamma}^{\mathrm{T}} \boldsymbol{C} \boldsymbol{\Gamma} \rangle \tag{9}$$

Work done on the laminate due to the applied compressive loading can be obtained using Eq. (10). Where n represents the total number of lamina layers, $T_i{}^l$ is the traction load applied, and w_i^l is the warping in the ith direction of the lth layer.

$$W = \sum_{l=1}^{l=n} T_i^l w_i^l(x_1, x_2, x_3) \tag{10}$$

Therefore, Eq. (11) gives the laminate's total potential energy.

$$\Pi = U - W \tag{11}$$

2.2.2. Warping constraints

The position vector representation includes rigid-body motions of the normal through the material points. Kinematic constraints in the form of warpings are necessary to exclude these rigid body motions. The warping constraint equations for an n-layered laminate are given in Eq. (12).

$$\sum_{l=1}^{l=n} \langle w_i^l(x_1, x_2, x_3) \rangle = 0 \qquad \sum_{l=1}^{l=n} \langle x_3 w_\alpha^l(x_1, x_2, x_3) \rangle = 0 \tag{12}$$

Thus, the potential energy functional is formulated by incorporating the warping constraints to the potential energy using the Lagrange multipliers (λ_i, λ_4, λ_5) as shown in Eq. (13). This study has a stiffened panel with eight layers of composite plate and a hat-stringer with seven layers. There will be 24 and 21 undetermined warpings in the respective potential energy functionals, which must be solved by minimising the derived energy functional based on the layup configuration.

$$\Pi^* = \Pi - \sum_{l=1}^{l=n} (\lambda_i \langle w_i^l(x_1, x_2, x_3) \rangle + \lambda_4 \langle x_3 w_1^l(x_1, x_2, x_3) \rangle + \lambda_5 \langle x_3 w_2^l(x_1, x_2, x_3) \rangle) \tag{13}$$

2.3. Dimensional reduction and two-dimensional constitutive law

Dimensional reduction is nothing but deriving an equivalent 2-D body over a 3-D body in the case of dimensionally reducible structures. This reduction is implemented by considering the geometrical and physical small parameters involved in the problem, such as thickness-to-length ratio (h/l) and strains in the current problem. Where h and l are the thickness and length of the structure, respectively. In order to obtain the asymptotically exact 2-D energy for the 3-D composite stiffened panel, identifying and ordering all the terms influencing the energy functional is a crucial step in the formulation. The energy functional written in Eq. (13) depends on material constants, thickness coordinate, 2-D strains, 3-D warpings, and their derivatives, *i.e.* $\Pi^* = \Pi^*$(material constants, $x_3, \epsilon_{\alpha\beta}, \kappa_{\alpha\beta}, \gamma_{\alpha 3}, w_i, w_{i,3}, w_{i,\alpha}$). Therefore, the dimensionally reduced model is obtained by ordering these terms in terms of the small parameter (δ) without any ad-hoc assumptions, unlike other existing traditional dimensional reduction methods.

Taking into account the leading order terms with a maximum contribution to the energy gives us the asymptotically exact energy functional. In this study, the energy functional order of magnitude up to $O(\delta^4)$ ensures up to zeroth order; the energy functional is accurate. Orders of the influencing parameters that give us energy functional of order $O(\delta^4)$ are as follows:

- $h/l \sim O(\delta_h)$
- $w_i \sim O(h\delta^2)$, $w_{i,\alpha} \sim O(\delta^2\delta_h)$, $w_{i,3} \sim O(\delta^2)$
- $\epsilon_{\alpha\beta} \sim O(\delta^2)$, $\gamma_{\alpha 3} \sim O(\delta^2)$, $\kappa_{\alpha\beta} \sim O(\delta^2)/h$

Where, δ_h is δ^4. The resulting functional obtained from this zeroth order approximation is denoted by Π_0. Using the variational calculus procedure, the unknown 3-D warpings are now obtained by minimising the energy functional Π_0. This minimisation $\delta\Pi_0 = 0$ results in Euler–Lagrange equations.

In the considered stiffened panel, the composite panel have eight plies, and the warpings of the individual plies resulting from solving the Euler–Lagrange equations will have 48 integration constants, which are unknowns, along with the five Euler–Lagrange constants. We need to ensure the inter-laminar continuity between the upper ply of the composite panel and the lower ply of the stiffener, resulting in additional equations along with the five warping constraints given in Eq. (12) to solve for the unknowns in the 3-D warping solutions. The warping continuity equations for the composite panel are as follows:

$$\begin{aligned} &[w_i^1 = w_i^2]_{x_3=3t} \quad [w_i^2 = w_i^3]_{x_3=2t} \quad [w_i^3 = w_i^4]_{x_3=t} \\ &\qquad\qquad [w_i^4 = w_i^5]_{x_3=0} \\ &[w_i^5 = w_i^6]_{x_3=-t} \quad [w_i^6 = w_i^7]_{x_3=-2t} \quad [w_i^7 = w_i^8]_{x_3=-3t} \end{aligned} \tag{14}$$

Similarly, the out-of-plane stress continuity equations between the plies of the panel are as follows:

$$\begin{aligned} &[\sigma_{i3}^1 = \sigma_{i3}^2]_{x_3=3t} \quad [\sigma_{i3}^2 = \sigma_{i3}^3]_{x_3=2t} \quad [\sigma_{i3}^3 = \sigma_{i3}^4]_{x_3=t} \\ &\qquad\qquad [\sigma_{i3}^4 = \sigma_{i3}^5]_{x_3=0} \\ &[\sigma_{i3}^5 = \sigma_{i3}^6]_{x_3=-t} \quad [\sigma_{i3}^6 = \sigma_{i3}^7]_{x_3=-2t} \quad [\sigma_{i3}^7 = \sigma_{i3}^8]_{x_3=-3t} \end{aligned} \tag{15}$$

The superscript in Eq. (14) and Eq. (15) represent the ply number, and t represents the thickness of individual ply. Similar continuity equations are written for the seven-layered hat-stringer to obtain the stringer's warpings. The resulting closed-form warping solutions obtained are a function of 2-D strains and are given in Appendix. Strain energy per unit area that is asymptotically correct for the stiffened panel in terms of 2-D strain measures is obtained by substituting these closed-form warpings solutions in the Π_0 and integrating over the thickness.

The 2-D constitutive law, presented in Eq. (16), is obtained by taking partial derivatives of the above-obtained Π_0 with respect to these 2-D strain measures. In the equation, $\boldsymbol{\epsilon}$, $\boldsymbol{\kappa}$, and $\boldsymbol{\gamma}$ are the strain

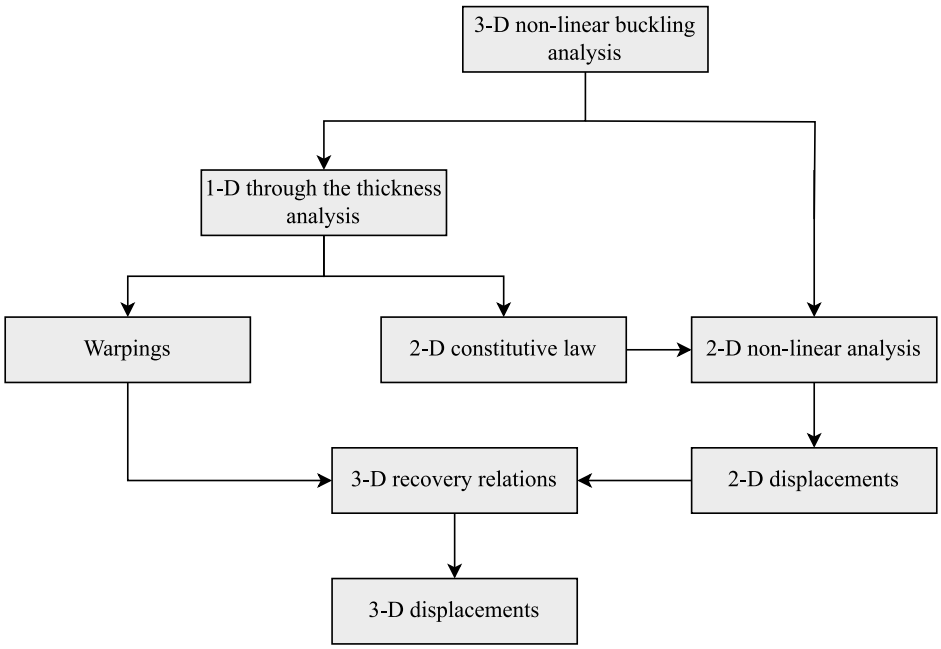

Fig. 3. Flowchart for non-linear buckling analysis of a composite plate using VAM formulation.

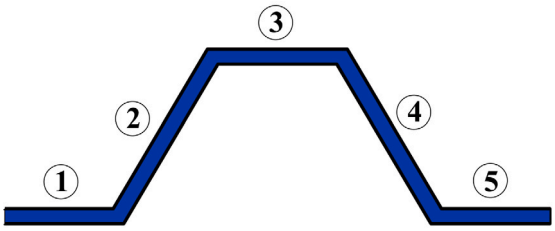

Fig. 4. Hat-stringer with five individual elements labelled on it.

measures, and the 2-D stiffness sub-matrices are **A**, **B**, **D**, and **G**.

$$\begin{pmatrix}\mathbf{N}\\ \mathbf{M}\\ \mathbf{Q}\end{pmatrix}=\begin{bmatrix}\mathbf{A} & \mathbf{B} & 0\\ \mathbf{B} & \mathbf{D} & 0\\ 0 & 0 & \mathbf{G}\end{bmatrix}\begin{pmatrix}\boldsymbol{\epsilon}\\ \boldsymbol{\kappa}\\ \boldsymbol{\gamma}\end{pmatrix} \tag{16}$$

Where the force (**N**), moment (**M**) and shear stress (**Q**) resultants are obtained using Eq. (17).

$$\mathbf{N}=\frac{\partial \Pi_0}{\partial \boldsymbol{\epsilon}},\quad \mathbf{M}=\frac{\partial \Pi_0}{\partial \boldsymbol{\kappa}},\quad \mathbf{Q}=\frac{\partial \Pi_0}{\partial \boldsymbol{\gamma}} \tag{17}$$

The above-mentioned methodology of dimensional reduction is implemented in Mathematica using the in-house code to obtain the equivalent zeroth order 2-D constitutive law for both the composite panel and the hat-stringer. The VAM formulation to perform the non-linear analysis is depicted in the flow chart given in Fig. 3. In this formulation, 3-D non-linear analysis will be performed by dividing the analysis into 1-D through the thickness analysis and 2-D non-linear analysis. The unknown warping solutions and the constitutive law can be obtained using the 1-D through the thickness analysis (refer Section 2.3). Using this equivalent constitutive law for the 3-D structure, the 2-D non-linear analysis is performed to obtain the 2-D displacement field. Later, the recovery relations can be used to obtain the displacement field of the structure by incorporating the warping solutions.

2.4. Constraint method and 2-D non-linear analysis

In this formulation, the novelty lies in ensuring the 3-D continuity of the laminated regions, excluding the delaminated regions of the 2-D components of the hat-stringer panel, using the constraint method. The constraint method is employed in two phases. The first phase occurs at the stringer level to ensure connectivity between the five components shown in Fig. 4. The second phase incorporates the connection between the laminated regions of the stringer feet and the panel, which differentiates the delaminated regions (DR) from the laminated regions (LR). The detailed mathematical procedure is explained in the flow chart given in Fig. 5. The 2-D non-linear analysis is performed by meshing both the stringer and the panel and using the equivalent 2-D constitutive laws of the stringer and plate obtained from the through-the-thickness analysis given in Section 2.3. Based on the elemental connectivity, the nodal connectivity in the laminated and delaminated regions is stored to attain the constraint matrix. The stiffened panel's initial displacement field (**U**) is given based on the imperfections obtained from the experiments. Then, the overall load is divided into n' number of load steps ($\Delta\mathbf{F} = \mathbf{F}/n'$); for each load step ($\Delta\mathbf{F}$), the global stiffness matrix is evaluated using the stringer and plate constraint matrices formulated based on the LR and DR of the stiffened panel. The 2-D displacement field is obtained using $\Delta\mathbf{U} = \mathbf{K}_g^{-1}\Delta\mathbf{F}$. Using the obtained displacement field, the corresponding internal force vector is obtained $\mathbf{F}_{\text{internal}}$. These iterations of calculating displacement field and internal force vector are carried out till the convergence criteria ($\Delta\mathbf{U} < 10^{-10}$) is reached. During these iteration processes, the 2-D displacement field obtained from each step is stored as $\mathbf{U} = \mathbf{U} + \Delta\mathbf{U}$. Further load steps are continued till the desired load (**F**) is reached. Then, the 3-D displacements are obtained using the recovery relations shown in Eq. (18), which are in terms of the 2-D displacements, rotations and warpings. In the entire formulation, ensuring the interactions between elements in the stringer and between the stringer and the panel is an integral part. The constraint matrices are formed by *ensuring 3-D displacement continuity* between the interface nodes in the laminated region.

$$\begin{bmatrix}U_1\\ U_2\\ U_3\end{bmatrix}=\begin{bmatrix}u_1\\ u_2\\ u_3\end{bmatrix}+x_3\begin{bmatrix}\theta_1\\ \theta_2\\ \theta_3\end{bmatrix}+C_{ij}w_j \tag{18}$$

Where U_i, u_i are 3-D, 2-D displacements, respectively. θ_i are the 2-D rotations, C_{ij} is the rotation matrix and w_j are the warpings. Ensuring the 3-D displacement continuity between the five elements of the stringer shown in Fig. 4 results in four different constraint matrices ($\boldsymbol{X}_{12}$, $\boldsymbol{X}_{23}$,

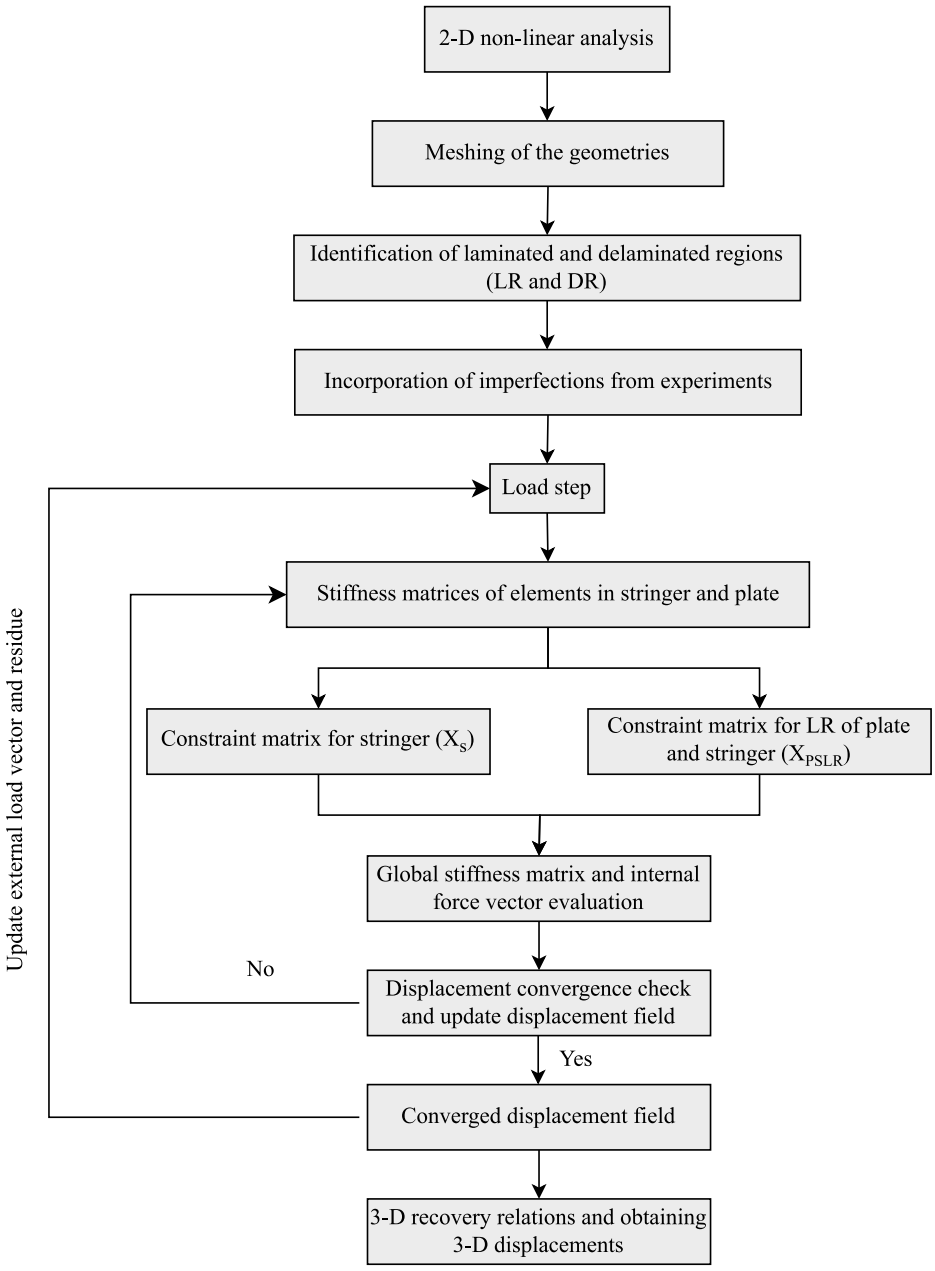

Fig. 5. 2-D non-linear analysis using the constraint method to analyse stiffened composite plate with delaminations.

$\boldsymbol{X}_{34}$, $\boldsymbol{X}_{45}$) relating the 2-D displacement fields. Eq. (19) provides the constraint matrices that ensure the connectivity of the five elements in the hat-stringer. Where $\boldsymbol{u}_{ⓘ}$ represents the 2-D displacement field of the individual stringer element ⓘ(refer Fig. 4). $\boldsymbol{X}_S$ represents the stringer constraint matrix, relating the 2-D displacement field of individual elements with the overall 2-D displacement field of the stringer (u_S). $\boldsymbol{X}_{12}, \boldsymbol{X}_{23}, \boldsymbol{X}_{34}, \boldsymbol{X}_{45}$ represent the individual constraint matrices relating the connection between individual elements (1–2; 2–3; 3–4 and 4–5) in the stringer as shown in Fig. 4.

$$\begin{pmatrix} \boldsymbol{u}_{①} \\ \boldsymbol{u}_{②} \\ \boldsymbol{u}_{③} \\ \boldsymbol{u}_{④} \\ \boldsymbol{u}_{⑤} \end{pmatrix} = [\boldsymbol{X}_S]\,(\boldsymbol{u}_S) \qquad [\boldsymbol{X}_S] = \begin{pmatrix} \boldsymbol{I} \\ \boldsymbol{X}_{12} \\ \boldsymbol{X}_{23} \\ \boldsymbol{X}_{34} \\ \boldsymbol{X}_{45} \end{pmatrix} \tag{19}$$

The procedure employed to attain stringer stiffness ($\boldsymbol{K}_S$) and force matrix ($\boldsymbol{F}_S$) using the constraint matrix is shown in Eq. (20). The stiffness matrix of the individual stringer element ⓘis represented using $\boldsymbol{K}_{ⓘ}$ and $\boldsymbol{F}_{ⓘ}$ represents the force vector of the individual stringer element ⓘ.

$$[\boldsymbol{K}_S] = \left[\boldsymbol{X}_S\right]^T \begin{bmatrix} \boldsymbol{K}_{①} & \boldsymbol{0} & \boldsymbol{0} & \boldsymbol{0} & \boldsymbol{0} \\ \boldsymbol{0} & \boldsymbol{K}_{②} & \boldsymbol{0} & \boldsymbol{0} & \boldsymbol{0} \\ \boldsymbol{0} & \boldsymbol{0} & \boldsymbol{K}_{③} & \boldsymbol{0} & \boldsymbol{0} \\ \boldsymbol{0} & \boldsymbol{0} & \boldsymbol{0} & \boldsymbol{K}_{④} & \boldsymbol{0} \\ \boldsymbol{0} & \boldsymbol{0} & \boldsymbol{0} & \boldsymbol{0} & \boldsymbol{K}_{⑤} \end{bmatrix} \left[\boldsymbol{X}_S\right] \qquad [\boldsymbol{F}_S] = \left[\boldsymbol{X}_S\right]^T \begin{bmatrix} \boldsymbol{F}_{①} \\ \boldsymbol{F}_{②} \\ \boldsymbol{F}_{③} \\ \boldsymbol{F}_{④} \\ \boldsymbol{F}_{⑤} \end{bmatrix} \tag{20}$$

Now, the continuity between plate and stringer in the laminated region (LR) is ensured at the 3-D level using the recovery relations given in Eq. (18), and the 2-D displacement fields of the plate ($\boldsymbol{u}_P$) and stringer ($\boldsymbol{u}_S$) are related with the 2-D displacement field of the stiffened

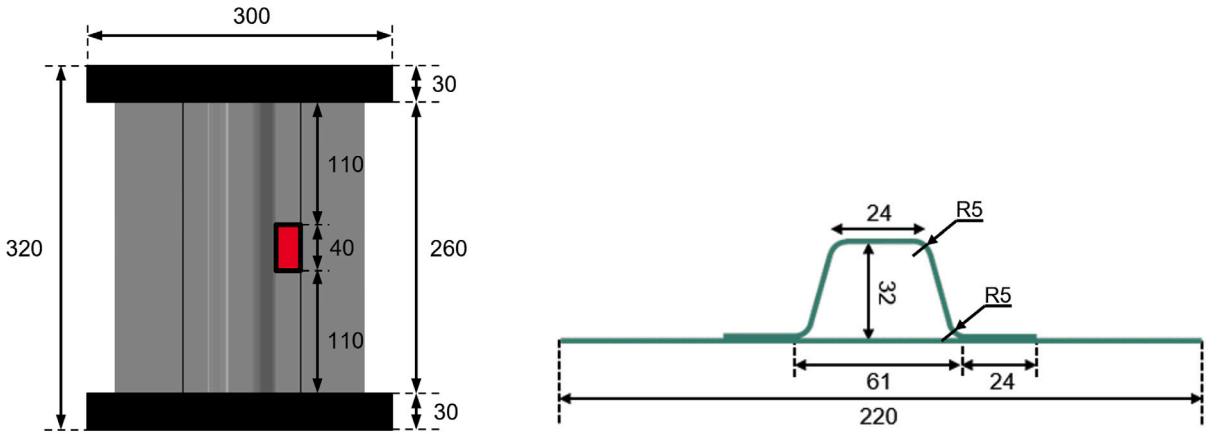

(a) Front view of the stiffened panel (b) Stiffened panel cross-section

Fig. 6. Nominal dimensions of the hat-stringer panel.

panel ($\boldsymbol{u}_{SP}$) using the constraint matrix $\boldsymbol{X}_{PSLR}$ as shown in Eq. (21). Subscripts S represents the stringer, and PSLR represents the plate-stringer-laminated region.

$$\begin{pmatrix} \boldsymbol{u}_S \\ \boldsymbol{u}_P \end{pmatrix} = [\boldsymbol{X}_{PSLR}]\,(\boldsymbol{u}_{SP}) \tag{21}$$

Now the global stiffness and force matrices are obtained using the constraint matrix as shown in Eq. (22). Here, $\boldsymbol{K}_g$ represents the global stiffness matrix of the stiffened panel. Where $\boldsymbol{K}_g$ is obtained using the constraint matrix and the individual stiffness matrix of the plate ($\boldsymbol{K}_P$) and stringer ($\boldsymbol{K}_S$). Similarly, Eq. (23) obtains the global force vector ($\boldsymbol{F}_g$). Where $\boldsymbol{F}_g$ is obtained using the constraint matrix and the individual force matrix of the plate ($\boldsymbol{F}_P$) and stringer ($\boldsymbol{F}_S$). Global stiffness matrix and global force vector are obtained using Newton–Raphson iterative procedure briefly depicted in Fig. 5.

$$[\boldsymbol{K}_g] = [\boldsymbol{X}_{PSLR}]^T \begin{bmatrix} \boldsymbol{K}_S & \boldsymbol{0} \\ \boldsymbol{0} & \boldsymbol{K}_P \end{bmatrix} [\boldsymbol{X}_{PSLR}] \tag{22}$$

$$[\boldsymbol{F}_g] = [\boldsymbol{X}_{PSLR}]^T \begin{bmatrix} \boldsymbol{F}_S \\ \boldsymbol{F}_P \end{bmatrix} \tag{23}$$

The above-developed C-VAM-based computational framework for the non-linear buckling analysis of dimensionally reduced stiffened panels is implemented using an in-house non-linear finite element solver in Mathematica.

3. Experiments and FEA modelling

The geometrical configurations of the stiffened panel considered for the current study are taken from the experimental work performed by Paz et al. [43], where a stiffened panel is tested experimentally with an initial delamination of 40 mm between the stringer and the skin. The results of the experiments and the 3-D FEA of the panel are used to validate the formulation described in Section 2. This section presents a comprehensive overview of the experiments conducted and the subsequent finite element analysis performed.

3.1. Stiffened panel description and test setup

The single-stringer panel from this work consists of a hat-stringer co-cured with the flat panel. The panel length and width are 320 mm and 220 mm, respectively. The stringer has the following dimensions: 32 mm in height, length and width, 320 mm and 109 mm, respectively. A Teflon insert of 40 mm is strategically positioned between the panel and the stringer feet to induce an initial delamination. Both ends of the panel are embedded in casting resin tabs with 30 mm in height for the application of axial loads, reducing the unsupported length of the stiffened panel to 260 mm. A front view of the panel is shown in Fig. 6(a), where the overall dimensions of the panel are indicated, the Teflon insert is coloured in red, and the resin tabs are depicted with solid black blocks. The panel's cross-section view, including the hat stiffener's dimensions, is shown in Fig. 6(b).

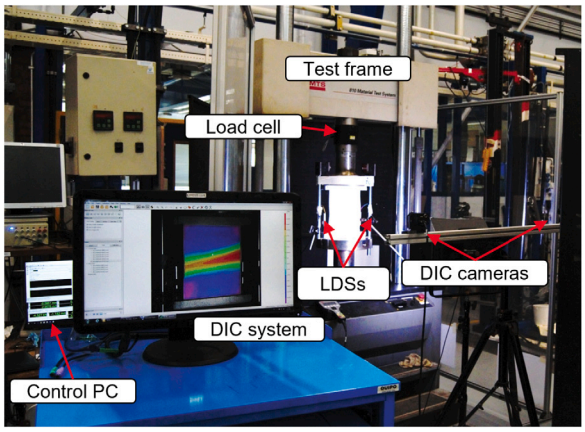

Fig. 7. Experimental test setup at Delft University of Technology showing the panel in a hydraulic universal testing machine together with the data acquisition used, such as the DIC and Laser displacement sensors (LDS).

Table 1
Material properties of IM7/8552 UD composite tape.

ρ [kg/m^3]	E_1 [GPa]	E_2 [GPa]	G_{12} [GPa]	G_{23} [GPa]	ν_{12}	ν_{23}
1570.00	146.00	8.20	5.20	3.90	0.32	0.45

The panel and the hat-stringer are made of IM7/8552 carbon-epoxy tape, where the individual thickness of each ply in the stiffened panel is 0.125 mm, and the material properties used for performing 3-D FEA are specified in Table 1. The in-plane properties are obtained from the experimental campaign reported in [44]. For the out-of-plane behaviour, it is assumed that $E_2 = E_3$, $G_{12} = G_{13}$, and $\nu_{12} = \nu_{13}$. The values for G_{13} and ν_{23} are taken from Krueger [45].

The panel is built as a quasi-isotropic layup with $[45/90/-45/0]_S$ orientation, while the hat-stringer is made up of a symmetric layup sequence of [−45/0/45/0/45/0/−45] orientation. Further details of the manufacturing and preparation of the panel prior to testing can be found in Paz et al. [43].

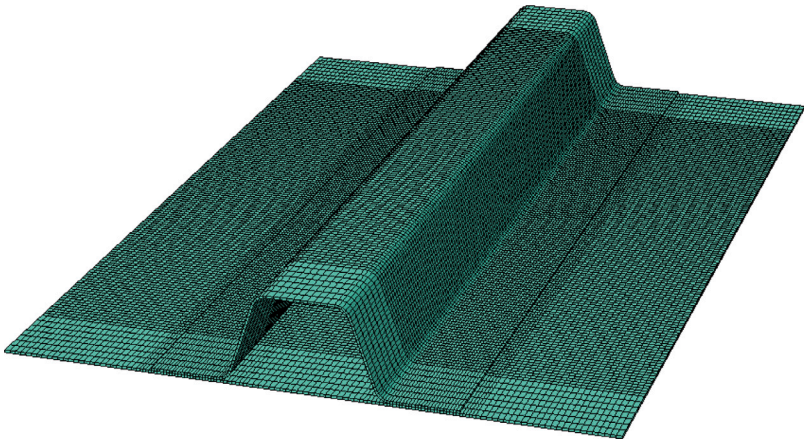

Fig. 8. Mesh of the finite element model of the hat-stringer panel containing 36000 hexahedral continuum shell elements.

The experimental test of the panel is conducted using a servo-hydraulic universal testing machine. The stiffened panel is tested under quasi-static compressive loads with displacement-controlled conditions at a 0.1 mm/min loading rate. The load–displacement response of the panel is retrieved from the machine's 500 kN load cell and displacement sensors. Two laser displacement sensors (LDS) are also placed on the opposite sides of the stiffened panel to verify that there is no load misalignment during testing. Moreover, two 3-D digital image correlation (DIC) is used to capture the displacements of the panel both from the panel and stringer sides. The DIC system is also used to capture the geometrical imperfections of the panel skin prior to testing that are later included in the C-VAM and FEA methods. Fig. 7 presents an image of the test setup.

3.2. Finite element modelling

Abaqus 2022 is used for creating and analysing the numerical model of the stiffened panel. The meshing of the model is done with 36000 linear hexahedral continuum shell elements with an edge size ranging from 1 mm for the free length to 4.3 mm for the area where the resin tabs are located. A detailed view of the meshed numerical model is presented in Fig. 8.

A constraint is applied to both ends of the numerical model to replicate the effect of the resin tabs, fixing all degrees of freedom of one end and only allowing for axial displacements of the other. The interface between the stringer and the panel is modelled with a tie constraint, releasing the nodes where the Teflon insert is placed. Until a load of 25.2 kN is reached, the upper end of the panel is displaced axially at a constant rate. This is done using a dynamic implicit step with a quasi-static application. Loads and displacements are obtained from the panel using a reference point at each end.

4. Results and discussion

This section presents the results of the non-linear buckling analysis of the delaminated stiffened panel conducted using the developed C-VAM formulation. In this section, C-VAM analysis results are verified with 3-D FEA to affirm the usage of the suggested methodology and compared with the experimental results. In addition to examining the global load–displacement response, this study compares the out-of-plane displacement contour plots and the variations in local out-of-plane displacements along both the pristine and delaminated sides of the stiffened panel.

4.1. Non-linear buckling analysis: Load–displacement response

The non-linear buckling analysis of the stiffened panel is conducted using the implemented in-house finite element program, which is based on the presented methodology. It is to be mentioned that the purpose of the analysis is not to investigate any damage evolution but to capture the buckling (primarily local) behaviour in such delaminated stiffened panels. This work does not consider any damage evolution apart from modelling the pre-existing delamination defects. Nonetheless, with a suitable damage modelling approach, such as incorporating a cohesive zone-based damage evolution, the C-VAM framework can be further expanded; nonetheless, such a significant task is set as the scope of further research.

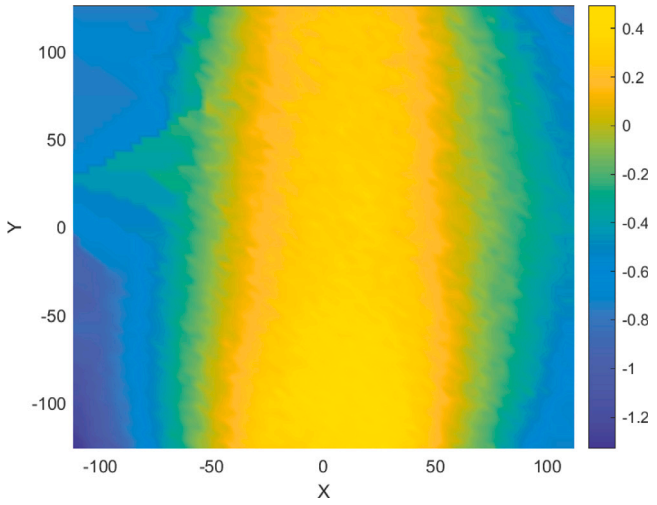

Fig. 9. Imperfection contour (in mm) along the length (−130 mm ≤ Y ≤ 130 mm) and width (−110 mm ≤ X ≤ 110 mm) of the hat-stringer panel with a delamination of 40 mm, retrieved from pre-test DIC measurements.

The initial imperfections of the panel are represented as the initial out-of-plane displacement field in the non-linear buckling analysis. Fig. 9 shows the imperfection field across the stiffened plate retrieved from the DIC measurements from the experiments. Later, a compressive load ranging from 0 kN to 25.2 kN is applied in multiple load steps to evaluate the panel displacements as well as obtain the complete 3-D deformation field using the recovery relations.

A mesh convergence study is carried out by varying the quad element size from 4 mm × 4 mm to 0.5 mm × 0.5 mm before performing the nonlinear buckling analysis using C-VAM. The convergence of the edge displacement under compressive loading of 25.2 kN at different mesh sizes is taken into account to finalise the mesh size. The plot depicting the mesh convergence is depicted in Fig. 10. For further analysis, the quad mesh size is fixed as 1 mm × 1 mm.

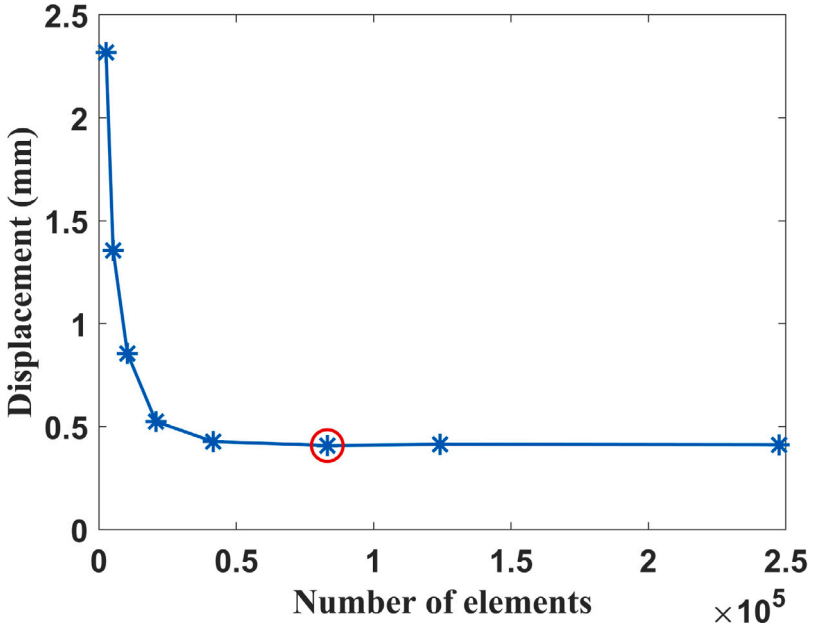

Fig. 10. Mesh convergence analysis: edge displacement variation with the increase in number of elements. The number of elements considered in the study is 83,120, circled in red in the convergence plot.

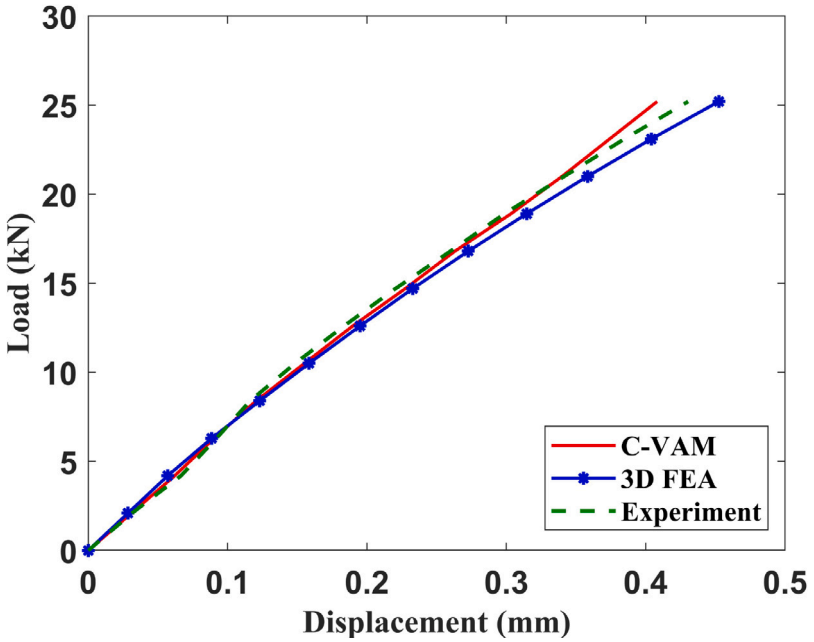

Fig. 11. Load vs displacement response of the hat-stringer panel with 40 mm delamination.

The load response plots obtained from C-VAM, experimental data and 3-D FEA are compared and shown in Fig. 11 to validate the formulation. The experimental and 3-D FEA results accord well with the VAM results. This validates the developed VAM formulation, which is a reliable approach for establishing the load–displacement behaviour of complex stiffened composite panels. One reason for the disparities between the VAM outcome and the FEA or experimental results under higher loads is that the VAM formulation currently employs a zeroth-order approximation; incorporating higher-order components could enhance precision at higher load levels. Nonetheless, a very good agreement can be observed with significantly reduced computational costs compared to the 3-D FEA, which presents the developed approach as a preferable choice for such analysis. Table 2 gives the displacement values at different loads to understand the variation in the results across the current approach (C-VAM), 3-D FEA and experimental results.

4.2. Buckled displacement and strain contours:

Comparison with experiments and 3-D FEA To observe the variation of the buckling shape of the stiffened panel with an increase in the compressive load, three different load levels, 15 kN, 20 kN and 25.2 kN, are considered. The out-of-plane displacement contours at different load levels are presented in Fig. 12. For comparing across the methods, the same scaling (in mm) has been used for all the load cases, *i.e.* [−4, 4]. It is identified that because of the delamination, the buckling shape is not symmetric about the centre of the stiffened

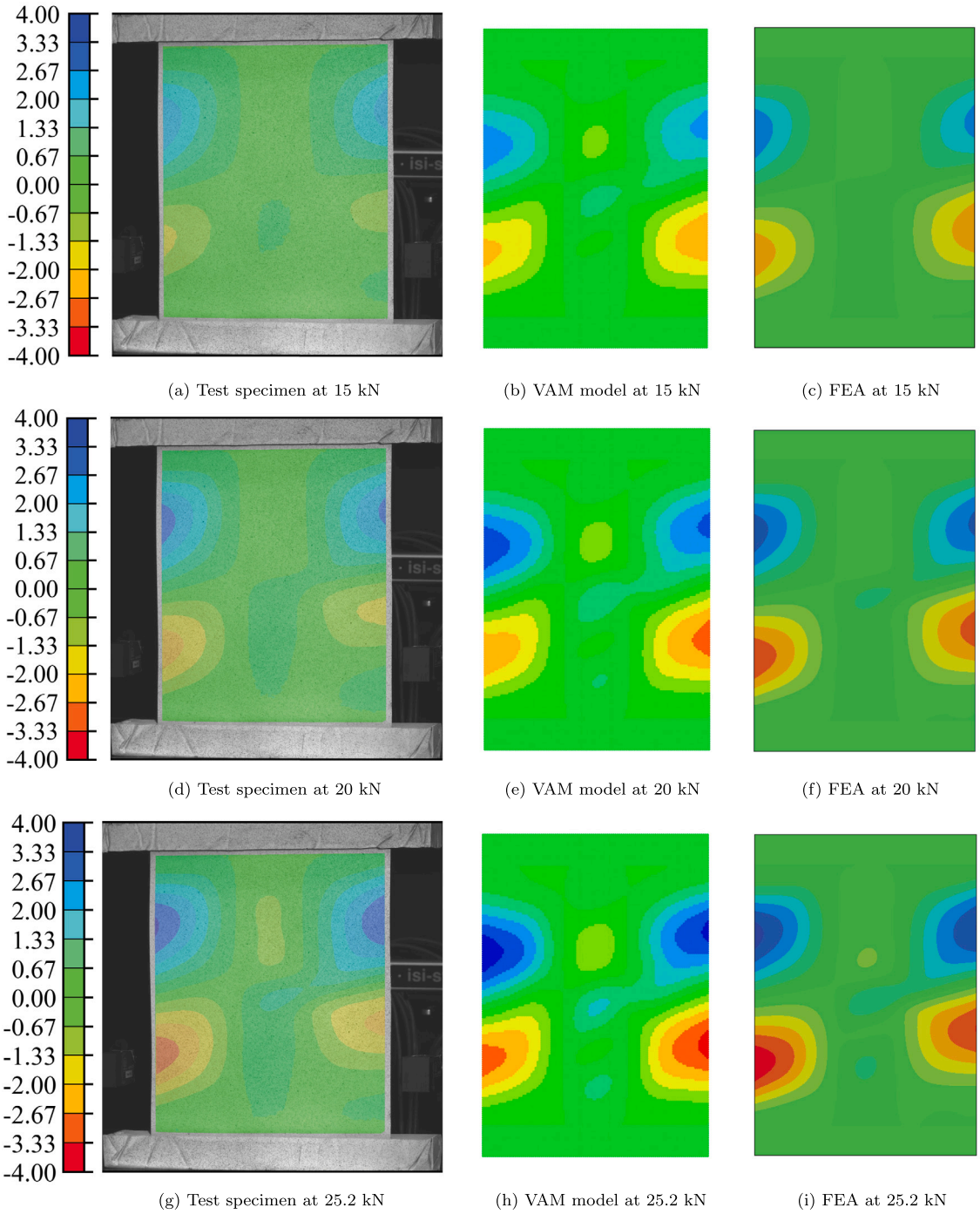

(a) Test specimen at 15 kN (b) VAM model at 15 kN (c) FEA at 15 kN

(d) Test specimen at 20 kN (e) VAM model at 20 kN (f) FEA at 20 kN

(g) Test specimen at 25.2 kN (h) VAM model at 25.2 kN (i) FEA at 25.2 kN

Fig. 12. Out-of-plane displacement data of the hat-stringer panel for the test specimen, VAM model, and FEA at three different load levels.

panel. On the delaminated side, the effective stiffness of the panel will be less compared to the opposite side, which results in higher deformation on the delamination side than the pristine side of the panel. In addition to the global response, the local displacement fields in the panel corresponding to local buckling are also captured well using the proposed approach are presented in the form of contour plots.

Figs. 12(a)–12(c) represents the contours at a load of 15 kN. In this case, it is observed that maximum out-of-plane displacements of 2.558 mm, around 2.595 mm and 2.624 mm are obtained from C-VAM, 3-D FEA and experiments, respectively. Maximum out-of-plane displacements of 3.280 mm, 3.230 mm and 3.124 mm are obtained from C-VAM, 3-D FEA and experiments, respectively, at a load of 20 kN (refer Figs. 12(d)–12(f)). Similarly, from Figs. 12(g)–12(i), we can identify that the maximum out-of-plane displacements are 3.940 mm, 3.877 mm and 3.479 mm using C-VAM, 3-D FEA and experiments, respectively, under the compressive load of 25.2 kN. The analysis is carried out only till 25.2 kN because, above this load, the delamination has started propagating towards the other foot of the stringer. Damage evolution has not been modelled in the currently proposed C-VAM formulation, which is beyond the scope of the current work and set as the scope of future work, so the results obtained from the current analysis above the damage propagation load will not be reliable. Along with the displacement contours, the strain contours have also been evaluated for comparison. For the sake of brevity, the strain contours are evaluated along longitudinal and transverse directions of the

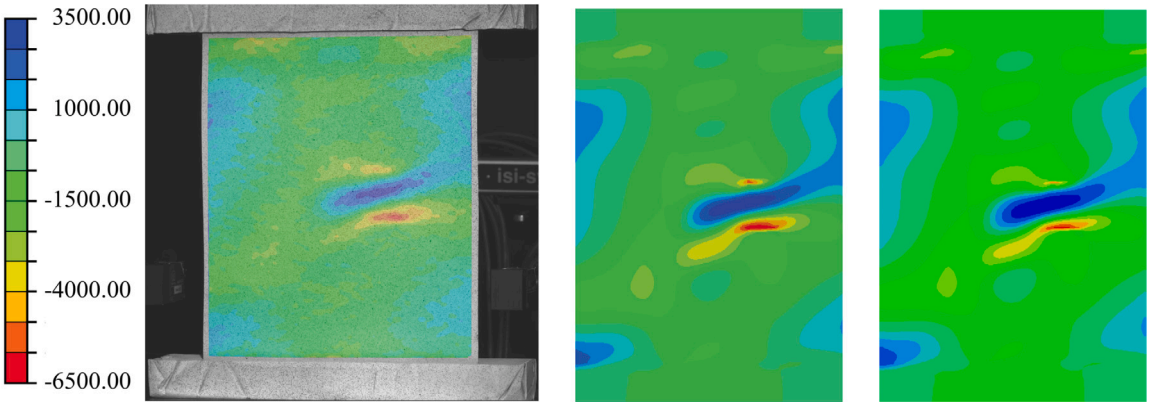

(a) Test specimen at 25.2 kN (b) FEA at 25.2 kN (c) VAM model at 25.2 kN

Fig. 13. Comparison of strain variation of the hat-stringer panel along the longitudinal direction from test specimen, FEA and VAM at 25.2 kN. Strain values are reported in microstrains.

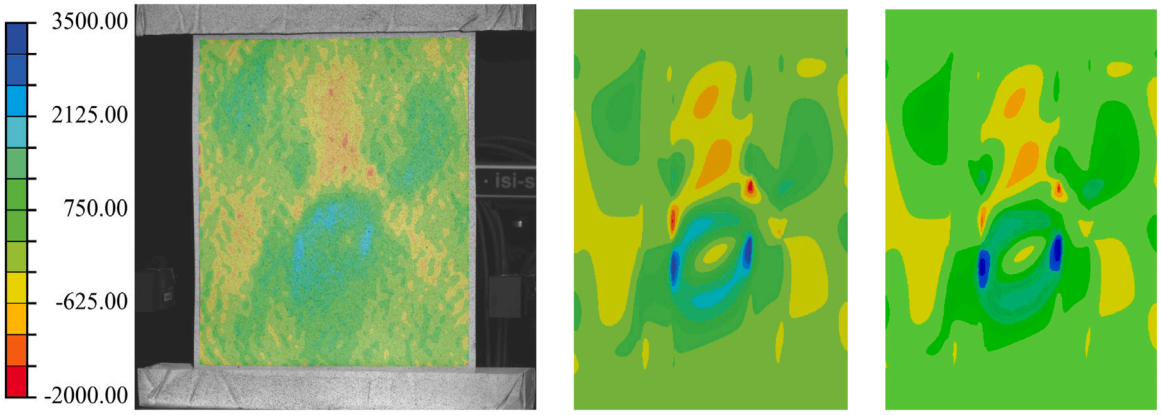

(a) Test specimen at 25.2 kN (b) FEA at 25.2 kN (c) VAM model at 25.2 kN

Fig. 14. Comparison of strain variation of the hat-stringer panel along the transverse direction from test specimen, FEA and VAM at 25.2 kN. Strain values are reported in microstrains.

Table 2
Displacements obtained from C-VAM, 3-D FEA, and experiments at different load levels.

Load (kN)	Displacement (mm)		
	C-VAM	3-D FEA	Experiment
06.3	0.0904	0.0886	0.0920
12.6	0.1898	0.1950	0.1835
18.9	0.3033	0.3146	0.2986
25.2	0.4080	0.4525	0.4304

stiffened panel along the panel side only at 25.2 kN loading. Figs. 13 and 14 represent the strain contours along longitudinal and transverse directions, respectively.

To have a better understanding and comparison of the out-of-displacements obtained from experiments, C-VAM and 3-D FEA, the displacement variation along the delaminated and pristine sides are extracted from the contours and presented in Fig. 15. There is a very good agreement observed in the displacement variation along the length at different load levels between C-VAM and 3-D FEA. However, when the results obtained from the experiments are compared with the analysis results, some disparities can be seen in the position of the maximum displacement location and the magnitude. These differences can be attributed to the following reasons: (1) Small geometrical and material imperfections that exist in the experiments. (2) The difference in the properties assigned for the laminates in the computational work might also be one of the reasons for this disparity at the local level. (3) Thermal loading has not been considered in both 3-D FEA and C-VAM analysis, but the specimen used in the experiments has undergone a curing cycle in the autoclave, which might develop interlaminar stress or residual stress between the plies or near the delamination zone. (4) Teflon insert, used in the specimen for creating the delamination, has not been modelled while conducting the computational analysis using 3-D FEA and C-VAM.

We can quantitatively compare the displacement variation by comparing the location and magnitude of maximum displacement along the pristine and delamination sides of the stiffened panel. From Fig. 15, it can be identified from VAM and 3-D FEA results show that the maximum out-of-plane displacement in the negative and positive Z directions is approximately 80 mm and 195 mm, respectively. When we look at the variation of the displacement obtained from experiments, even though there are variations in the magnitude of the displacements, the location of the maximum displacements is close to the results obtained from VAM and 3-D FEA along the pristine side of the stiffened panel.

Along the pristine side, the half-wave variation obtained from 3-D FEA and experiments is close to the variation obtained from C-VAM for all three load cases. However, along the delaminated side, the variations obtained from C-VAM are close to the other two methods on the upper half of the stiffened panel. A comparison of the results between C-VAM and 3-D FEA shows very good agreement. Major

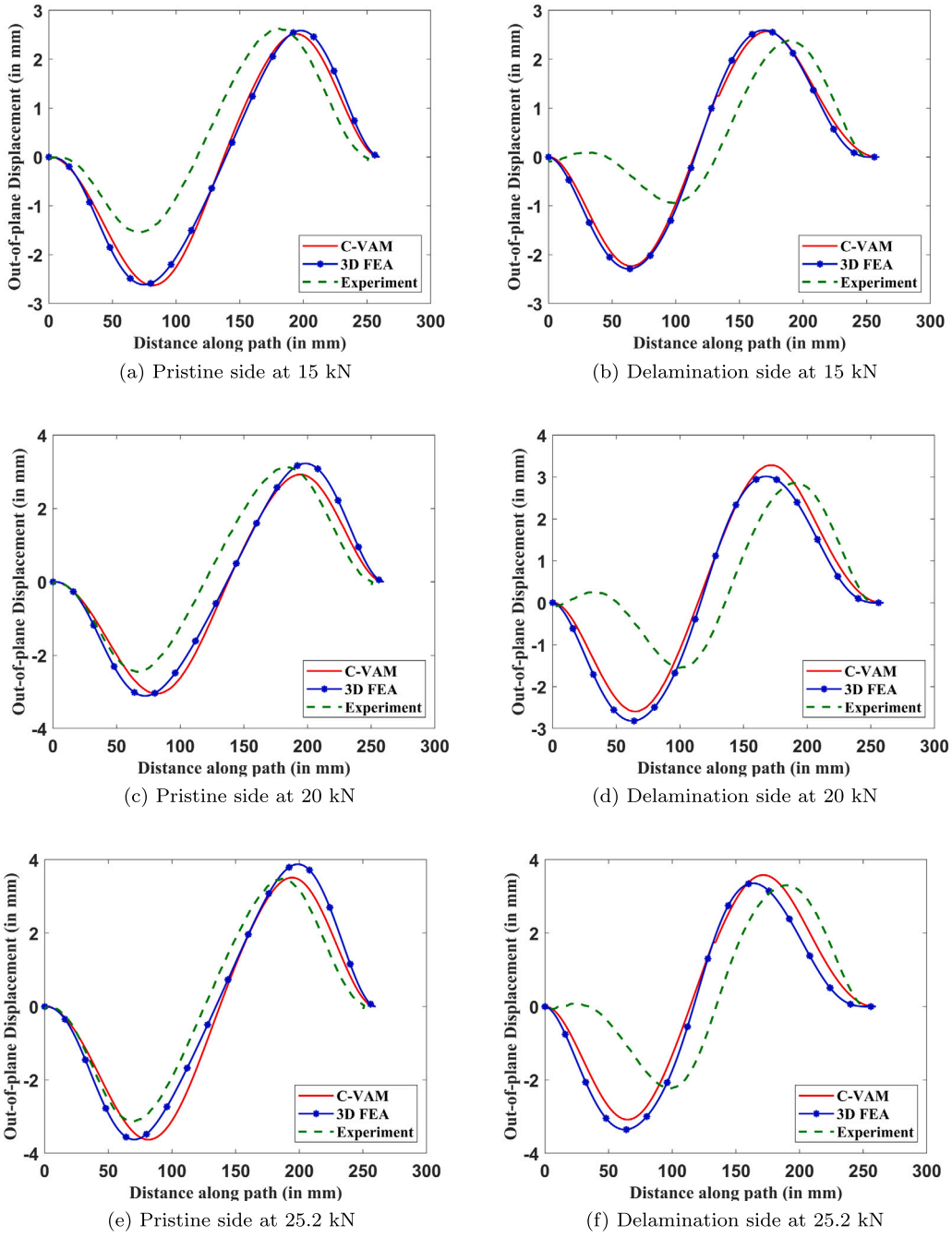

(a) Pristine side at 15 kN (b) Delamination side at 15 kN

(c) Pristine side at 20 kN (d) Delamination side at 20 kN

(e) Pristine side at 25.2 kN (f) Delamination side at 25.2 kN

Fig. 15. Out-of-plane displacement variation along the free edges of the hat-stringer panel at different load levels.

variation can be observed only along the lower half of the panel when compared with experimental results.

Computational time:

The proposed methodology is advantageous over 3-D FEA in terms of the computational cost while providing a similar level of accuracy. This is especially true when using non-linear methods to analyse complex structures like hat-stringer panels with delamination defects. Below, we compare the computational time associated with the non-linear analyses conducted in this work using 3-D FEA and C-VAM formulation. The analyses were run on a computer with an Intel i7 processor of speed 200 GHz and a RAM of 32 GB.

The computational time for 3-D FEA and C-VAM are approximately 67 min and 30 min, respectively. The computational efficiency is as high as nearly 55% at a maximum load of 25.20 kN. As the structural system gets more complex with multiple delaminated regions and multiple stringers, this computational cost reduction will be even more significant than the existing methodologies.

5. Conclusions

In this study, a comprehensive analysis of a delaminated hat-stringer composite panel is carried out to evaluate the buckling behaviour under compressive loads, utilising a combination of constraint variational asymptotic method (C-VAM), 3-D finite element analysis (FEA), and experimental testing. The investigation aimed to validate the developed C-VAM formulation as a reliable method for predicting the

load–displacement and buckling behaviour of the stiffened composite panels containing pre-existing delamination defects. The following conclusions are arrived at:

- The load response plot obtained from the C-VAM formulation was found to be in good agreement with the 3-D FEA and experimental results, validating that this can be used as a reliable method for predicting the load–displacement behaviour of delaminated stiffened panels.
- The out-of-plane displacement variation obtained from C-VAM matches very well with that of the 3-D FEA. The results are also close to the variation obtained from experiments along the pristine side of the stiffened panel, especially at higher loads.
- Along the delaminated side, the out-of-plane displacement variation obtained from C-VAM was close to that of the other two methods on the upper half of the stiffened panel. However, major variation can be observed along the lower half of the panel.
- The proposed methodology is shown to be computationally efficient by over 55% when compared with 3-D FEA while providing similar accuracy for the non-linear buckling analysis.

Overall, a very good agreement was observed, both at the level of global response and the local buckling deformation contours across C-VAM, 3-D FEA, and experimental results. Some disparities were observed in the experimental results. The proposed formulation will be expanded to account for damage evolution, forming the scope for further research.

CRediT authorship contribution statement

A. Phanendra Kumar: Writing – original draft, Validation, Software, Methodology, Investigation, Formal analysis. **Javier Paz Méndez:** Writing – original draft, Validation, Software, Methodology. **Ramesh Gupta Burela:** Writing – review & editing, Resources, Methodology. **Chiara Bisagni:** Writing – review & editing, Supervision, Resources, Project administration, Funding acquisition, Conceptualization. **Dineshkumar Harursampath:** Writing – review & editing, Supervision, Resources, Project administration, Funding acquisition, Conceptualization. **Sathiskumar Anusuya Ponnusami:** Writing – review & editing, Supervision, Project administration, Methodology, Funding acquisition, Conceptualization.

Declaration of competing interest

The authors declare that they have no known competing financial interests or personal relationships that could have appeared to influence the work reported in this paper.

Data availability

Data will be made available on request.

Acknowledgements

The authors would like to acknowledge the financial support provided by the IISc-TU Delft Collaborative Research Grant program. The first author would like to extend the acknowledgement to the Prime Minister's Research Fellowship Scheme, India, for the support during the research.

Appendix A. Analytical solutions for the warping functions in the plate and the stringer

Using the C-VAM formulation, closed-form solutions are obtained for the warpings and stiffness matrix coefficients for all the hat-stringer and plate composite layers. Closed-form warping equations obtained in terms of individual layer material constants and the thickness of the plies take up more space. Therefore, simplified expressions are presented in the appendix. In the below equations, subscripts represent the warping direction, and the superscripts represent the layer number. Hat-stringer and plate consist of seven and eight layers, respectively (see Boxes II–IV, I and V).

$$
\left.
\begin{aligned}
w_1^{L1} &= \gamma_{13}\left(-4.745x_3^3 - 1.429\times10^{-16}x_3^2 + 15.428x_3 - 4.743\right)\\
&\quad + \gamma_{23}\left(-0.833x_3^3 - 2.422\times10^{-17}x_3^2 + 0.478x_3 - 0.128\right)\\
w_2^{L1} &= \gamma_{13}\left(75.549x_3^3 - 6.514\times10^{-17}x_3^2 - 50.932x_3 - 4.044\right)\\
&\quad + \gamma_{23}\left(-0.036x_3^3 - 1.358\times10^{-15}x_3^2 + 0.359x_3 + 0.041\right)\\
w_3^{L1} &= -0.002\gamma_{12} + 1.084\times10^{-19}\gamma_{21} + 0.015\kappa_{11} - 0.0002\left(\kappa_{12}+\kappa_{21}\right) + 0.015\kappa_{22} +\\
&\quad + x_3^2\left(2.430\times10^{-19}\gamma_{12} - 0.231\kappa_{11} + 0.002\left(\kappa_{12}+\kappa_{21}\right) - 0.231\kappa_{22}\right)\\
&\quad + x_3\left(0.002\gamma_{12} + 0.002\gamma_{21} - 1.361\times10^{-17}\kappa_{22} - 0.462\epsilon_{11} - 0.462\epsilon_{22}\right)\\
&\quad - 0.0008\epsilon_{11} + 0.0008\epsilon_{22}\\
w_1^{L2} &= \gamma_{13}\left(-4.036x_3^3 + 1.104\times10^{-16}x_3^2 + 0.318x_3 + 0.904\right)\\
&\quad + \gamma_{23}\left(-0.215x_3^3 - 9.005\times10^{-18}x_3^2 + 0.123x_3 - 0.036\right)\\
w_2^{L2} &= \gamma_{13}\left(87.111x_3^3 - 9.547\times10^{-17}x_3^2 - 58.650x_3 - 2.472\right)\\
&\quad + \gamma_{23}\left(-1.550\times10^{-15}x_3^2 + 0.673x_3 - 0.041\right)\\
w_3^{L2} &= -0.00004\left(\kappa_{12}+\kappa_{21}\right) + 0.015\kappa_{22} + \gamma_{12}\left(2.430\times10^{-19}x_3^2 - 0.002x_3 - 0.0005\right)\\
&\quad + \gamma_{21}\left(0.002x_3 + 1.151\times10^{-19}\right) - 0.233\kappa_{11}x_3^2 - 0.229\kappa_{22}x_3^2\\
&\quad - 0.467x_3\epsilon_{11} - 0.458x_3\epsilon_{22} + 0.0005\epsilon_{11} - 0.0005\epsilon_{22} + 0.015\kappa_{11}
\end{aligned}
\right\}\ \text{Hat-stringer's warping functions}
$$

Box I.

$$
\begin{aligned}
w_1^{L3} &= \gamma_{13}\left(-15.598x_3^3 + 1.407\times10^{-16}x_3^2 + 8.035x_3 - 0.243\right)\\
&\quad + \gamma_{23}\left(-0.251x_3^3 + 1.833\times10^{-16}x_3^2 - 0.190x_3 + 0.019\right)\\
w_2^{L3} &= \gamma_{13}\left(76.895x_3^3 - 1.019\times10^{-16}x_3^2 - 51.7048x_3 - 3.48341\right)\\
&\quad + \gamma_{23}\left(0.0358309x_3^3 - 1.355\times10^{-15}x_3^2 + 0.318219x_3 + 0.0220172\right)\\
w_3^{L3} &= 0.0002\gamma_{12} + 2.878\times10^{-20}\gamma_{21} + 0.015\kappa_{11} + 0.00002\left(\kappa_{12}+\kappa_{21}\right)\\
&\quad + 0.015\kappa_{22} + x_3^2\left(2.430\times10^{-19}\gamma_{12} - 0.231\kappa_{11} - 0.002\left(\kappa_{12}+\kappa_{21}\right) - 0.231\kappa_{22}\right)\\
&\quad + x_3\left(-0.006\gamma_{12} + 0.002\gamma_{21} - 4.083\times10^{-17}\kappa_{11} - 0.462\epsilon_{11}\right)\\
&\quad - 0.0002\epsilon_{11} + 0.0002\epsilon_{22} - 0.462\epsilon_{22}y_3\\
w_1^{L4} &= \gamma_{13}\left(-4.036x_3^3 + 1.104\times10^{-16}x_3^2 + 0.317x_3 + 0.206\right)\\
&\quad + \gamma_{23}\left(-0.215x_3^3 - 9.005\times10^{-18}x_3^2 + 0.123x_3 - 3.927\times10^{-18}\right)\\
w_2^{L4} &= \gamma_{13}\left(87.111x_3^3 - 9.547\times10^{-17}x_3^2 - 58.649x_3 - 3.082\right)\\
&\quad + \gamma_{23}\left(-1.550\times10^{-15}x_3^2 + 0.672908x_3 + 9.090\times10^{-17}\right)\\
w_3^{L4} &= 0.015\kappa_{11} + 0.00001\left(\kappa_{12}+\kappa_{21}\right) + 0.015\kappa_{22} - 0.458388\epsilon_{22}x_3\\
&\quad + x_3\left(0.002\gamma_{21} - 1.361\times10^{-17}\kappa_{11} + 1.361\times10^{-17}\kappa_{22} - 0.466684\epsilon_{11}\right)\\
&\quad + \gamma_{12}\left(2.430\times10^{-19}x_3^2 - 0.00207412x_3 - 1.171\right) + \left(-0.233\kappa_{11} - 0.229\kappa_{22}\right)x_3^2\\
w_1^{L5} &= \gamma_{13}\left(-15.598x_3^3 + 1.407\times10^{-16}x_3^2 + 8.035x_3 + 0.721\right)\\
&\quad + \gamma_{23}\left(-0.251x_3^3 + 1.833\times10^{-16}x_3^2 - 0.190x_3 - 0.019\right)\\
w_2^{L5} &= \gamma_{13}\left(76.895x_3^3 - 1.019\times10^{-16}x_3^2 - 51.705x_3 - 2.615\right)\\
&\quad + \gamma_{23}\left(0.036x_3^3 - 1.355\times10^{-15}x_3^2 + 0.318x_3 - 0.022\right)\\
w_3^{L5} &= -0.0002\gamma_{12} - 3.598\times10^{-16}\gamma_{21} + 0.015\kappa_{11} + 0.00002\left(\kappa_{12}+\kappa_{21}\right) + 0.015\kappa_{22}\\
&\quad + x_3^2\left(-0.231\kappa_{11} - 0.002\left(\kappa_{12}+\kappa_{21}\right) - 0.231\kappa_{22}\right) - 0.0002\epsilon_{22} + 0.0002\epsilon_{11}\\
&\quad + x_3\left(-0.006\gamma_{12} + 0.002\gamma_{21} - 4.083\times10^{-17}\kappa_{11} - 0.462\epsilon_{11} - 0.462\epsilon_{22}\right)\\
w_1^{L6} &= \gamma_{13}\left(-4.036x_3^3 + 1.104\times10^{-16}x_3^2 + 0.318x_3 - 1.017\right)\\
&\quad + \gamma_{23}\left(-0.215x_3^3 - 9.005\times10^{-18}x_3^2 + 0.123x_3 + 0.036\right)\\
w_2^{L6} &= \gamma_{13}\left(87.111x_3^3 - 9.547\times10^{-17}x_3^2 - 58.650x_3 - 4.217\right)\\
&\quad + \gamma_{23}\left(-1.550\times10^{-15}x_3^2 + 0.673x_3 + 0.040\right)\\
w_3^{L6} &= 0.015\kappa_{11} - 0.00004\left(\kappa_{12}+\kappa_{21}\right) + 0.015\kappa_{22} + \gamma_{12}\left(2.430\times10^{-19}x_3^2 - 0.002x_3\right)\\
&\quad + \gamma_{21}\left(0.00207412x_3 - 3.598\times10^{-20}\right) - 0.233\kappa_{11}x_3^2 - 0.229\kappa_{22}x_3^2 + 0.0005\gamma_{21}\\
&\quad - 0.466x_3\epsilon_{11} - 0.458x_3\epsilon_{22} - 0.0005\epsilon_{11} + 0.0005\epsilon_{22} - 3.402\times10^{-17}\kappa_{11}x_3\\
w_1^{L7} &= \gamma_{13}\left(6.179x_3^3 + 1.168\times10^{-16}x_3^2 + 8.07649x_3 + 0.565\right)\\
&\quad + \gamma_{23}\left(-0.251x_3^3 - 2.043\times10^{-16}x_3^2 + 0.478x_3 + 0.128\right)\\
w_2^{L7} &= \gamma_{13}\left(75.549x_3^3 - 6.514\times10^{-17}x_3^2 + 51.992x_3 + 31.159\right)\\
&\quad + \gamma_{23}\left(-0.0358x_3^3 - 1.358\times10^{-15}x_3^2 + 0.359x_3 - 0.041\right)\\
w_3^{L7} &= 0.002\gamma_{12} + 0.015\kappa_{11} - 0.0002\left(\kappa_{12}+\kappa_{21}\right) + 0.015\kappa_{22} + 0.0008\epsilon_{11} - 0.0008\epsilon_{22}\\
&\quad + x_3^2\left(2.430\times10^{-19}\gamma_{12} - 0.231\kappa_{11} + 0.002\left(\kappa_{12}+\kappa_{21}\right) - 0.231\kappa_{22}\right)\\
&\quad + x_3\left(0.002\gamma_{12} + 0.002\gamma_{21} + 1.361\times10^{-17}\kappa_{22} - 0.462\epsilon_{11} - 0.462\epsilon_{22}\right)
\end{aligned}
\Bigg\}\ \text{Hat-stringer's warping functions}
$$

Box II.

$$
\begin{aligned}
w_1^{L1} &= \gamma_{13}\left(5.717x_3^3 + 0.00007x_3^2 + 0.624x_3 - 0.024\right)\\
&\quad + \gamma_{23}\left(0.173x_3^3 - 0.014x_3^2 - 0.459x_3 + 0.144\right)\\
w_2^{L1} &= \gamma_{13}\left(-63.889x_3^3 + 0.016x_3^2 - 0.483x_3 + 0.152\right)\\
&\quad + \gamma_{23}\left(-0.025x_3^3 - 0.0004x_3^2 + 0.427x_3 + 0.009\right)\\
w_3^{L1} &= 0.019\kappa_{11} + 0.0003\kappa_{12} + 0.0003\kappa_{21} + 0.019\kappa_{22} - 4.899\times10^{-17}\kappa_{22}x_3\\
&\quad + \gamma_{12}\left(-0.002x_3 + 0.001\right) + \gamma_{21}\left(-0.002x_3 + 0.001\right)\\
&\quad - 0.231\kappa_{11}x_3^2 - 0.002\kappa_{12}x_3^2 - 0.002\kappa_{21}x_3^2 - 0.231\kappa_{22}x_3^2\\
&\quad - 5.551\times10^{-17}\kappa_{11}x_3 + 4.337\times10^{-19}\kappa_{12}x_3 + 4.337\times10^{-19}\kappa_{21}x_3\\
&\quad - 0.462x_3\epsilon_{11} - 0.462x_3\epsilon_{22} + 1.605\times10^{-17}\epsilon_{11} + 1.171\times10^{-17}\epsilon_{22}\\
w_1^{L2} &= \gamma_{13}\left(-0.3978x_3^3 + 0.003x_3^2 + 0.980x_3 - 0.133\right)\\
&\quad + \gamma_{23}\left(1.980\times10^{-1}x_3^3 - 1.686\times10^{-2}x_3^2 - 1.316x_3 + 4.386\times10^{-2}\right)\\
w_2^{L2} &= \gamma_{13}\left(-5.519\times10^{-2}x_3^3 + 1.369\times10^{-2}x_3^2 - 9.492\times10^{-2}x_3 + 3.347\times10^{-2}\right)\\
&\quad + \gamma_{23}\left(-2.172\times10^{-3}x_3^2 + 6.603\times10^{-2}x_3 + 1.194\times10^{-1}\right)\\
w_2^{L2} &= 0.01908\kappa_{11} + 6.482\times10^{-5}\kappa_{12} + 6.482\times10^{-5}\kappa_{21} + 0.01947\kappa_{22}\\
&\quad + \gamma_{12}\left(1.276\times10^{-19}x_3^2 + 1.276\times10^{-19}x_3 + 2.593\times10^{-4}\right)\\
&\quad + \gamma_{21}\left(1.276\times10^{-19}x_3^2 + 1.276\times10^{-19}x_3 + 2.593\times10^{-4}\right)\\
&\quad - 0.2292\kappa_{11}x_3^2 - 5.104\times10^{-19}\kappa_{12}x_3^2 - 5.104\times10^{-19}\kappa_{21}x_3^2 - 0.2333\kappa_{22}x_3^2\\
&\quad + 5.104\times10^{-19}\kappa_{12}x_3 + 5.104\times10^{-19}\kappa_{21}x_3 - 1.633\times10^{-17}\kappa_{22}x_3\\
&\quad - 0.4584x_3\epsilon_{11} - 0.4667x_3\epsilon_{22} - 1.556\times10^{-3}\epsilon_{11} + 1.556\times10^{-3}\epsilon_{22}\\
w_1^{L3} &= \gamma_{13}\left(-1.268\times10^{1}x_3^3 + 4.638\times10^{-3}x_3^2 + 5.924\times10^{-1}x_3 - 4.400\times10^{-2}\right)\\
&\quad + \gamma_{23}\left(1.732\times10^{-1}x_3^3 - 1.512\times10^{-2}x_3^2 + 2.292\times10^{-1}x_3 - 3.889\times10^{-2}\right)\\
w_2^{L3} &= \gamma_{13}\left(-6.4884\times10^{1}x_3^3 + 1.6305\times10^{-2}x_3^2 + 2.6183\times10^{-1}x_3 - 4.8397\times10^{-2}\right)\\
&\quad + \gamma_{23}\left(2.4745\times10^{-2}x_3^3 - 4.6414\times10^{-3}x_3^2 + 3.9392\times10^{-1}x_3 + 4.4364\times10^{-2}\right)\\
w_3^{L3} &= 0.01921\kappa_{11} - 6.482\times10^{-5}\kappa_{12} - 6.482\times10^{-5}\kappa_{21} + 0.01934\kappa_{22}\\
&\quad + \gamma_{12}\left(1.276\times10^{-19}x_3^2 + 2.074\times10^{-3}x_3 - 2.593\times10^{-4}\right)\\
&\quad + \gamma_{21}\left(1.276\times10^{-19}x_3^2 + 2.074\times10^{-3}x_3 - 2.593\times10^{-4}\right)\\
&\quad - 0.23127\kappa_{11}x_3^2 + 2.074\times10^{-3}\kappa_{12}x_3^2 + 2.074\times10^{-3}\kappa_{21}x_3^2 - 0.23127\kappa_{22}x_3^2\\
&\quad - 3.266\times10^{-17}\kappa_{11}x_3 - 5.104\times10^{-19}\kappa_{12}x_3 - 5.104\times10^{-19}\kappa_{21}x_3\\
&\quad - 0.46254x_3\epsilon_{11} - 0.46254x_3\epsilon_{22} - 5.185\times10^{-4}\epsilon_{11} + 5.185\times10^{-4}\epsilon_{22}\\
w_1^{L4} &= \gamma_{13}\left(-2.983\times10^{0}x_3^3 + 2.021\times10^{-3}x_3^2 + 2.356\times10^{-1}x_3 - 2.835\times10^{-4}\right)\\
&\quad + \gamma_{23}\left(1.4847\times10^{-1}x_3^3 - 1.265\times10^{-2}x_3^2 - 9.8706\times10^{-2}x_3 + 1.206\times10^{-3}\right)\\
w_2^{L4} &= \gamma_{13}\left(-7.3585\times10^{1}x_3^3 + 1.825\times10^{-2}x_3^2 - 1.266\times10^{-1}x_3 - 8.9303\times10^{-4}\right)\\
&\quad + \gamma_{23}\left(-2.8957\times10^{-3}x_3^2 + 7.5471\times10^{-1}x_3 + 1.8235\times10^{-4}\right)
\end{aligned}
\Bigg\}\ \text{Plate's warping functions}
$$

Box III.

$$
\begin{aligned}
w_3^{L4} &= 0.01924\kappa_{11} - 3.2408\times10^{-5}\kappa_{12} - 3.2408\times10^{-5}\kappa_{21} + 0.01930\kappa_{22} \\
&\quad + \gamma_{12}\left(1.276\times10^{-19}x_3^2 + 1.276\times10^{-19}x_3 - 2.711\times10^{-20}\right) \\
&\quad + \gamma_{21}\left(1.276\times10^{-19}x_3^2 + 1.276\times10^{-19}x_3 - 2.711\times10^{-20}\right) \\
&\quad - 0.23334\kappa_{11}x_3^2 - 5.104\times10^{-19}\kappa_{12}x_3^2 - 5.104\times10^{-19}\kappa_{21}x_3^2 \\
&\quad - 0.22919\kappa_{22}x_3^2 + 1.633\times10^{-17}\kappa_{11}x_3 + 1.633\times10^{-17}\kappa_{22}x_3 \\
&\quad - 0.46668x_3\epsilon_{11} - 0.45839x_3\epsilon_{22} + 3.226\times10^{-18}\epsilon_{11} + 3.198\times10^{-18}\epsilon_{22} \\
w_1^{L5} &= \gamma_{13}\left(-2.983\times10^{0}x_3^3 + 2.021\times10^{-3}x_3^2 + 2.356\times10^{-1}x_3 - 2.835\times10^{-4}\right) \\
&\quad + \gamma_{23}\left(1.4847\times10^{-1}x_3^3 - 1.265\times10^{-2}x_3^2 - 9.8706\times10^{-2}x_3 + 1.206\times10^{-3}\right) \\
w_2^{L5} &= \gamma_{13}\left(-7.3585\times10^{1}x_3^3 + 1.825\times10^{-2}x_3^2 - 1.266\times10^{-1}x_3 - 8.9303\times10^{-4}\right) \\
&\quad + \gamma_{23}\left(-2.8957\times10^{-3}x_3^2 + 7.5471\times10^{-1}x_3 + 1.8235\times10^{-4}\right) \\
w_3^{L5} &= 0.01924\kappa_{11} - 3.2408\times10^{-5}\kappa_{12} - 3.2408\times10^{-5}\kappa_{21} + 0.01930\kappa_{22} \\
&\quad + \gamma_{12}\left(1.276\times10^{-19}x_3^2 + 1.276\times10^{-19}x_3 - 2.711\times10^{-20}\right) \\
&\quad + \gamma_{21}\left(1.276\times10^{-19}x_3^2 + 1.276\times10^{-19}x_3 - 2.711\times10^{-20}\right) \\
&\quad - 0.23334\kappa_{11}x_3^2 - 5.104\times10^{-19}\kappa_{12}x_3^2 - 5.104\times10^{-19}\kappa_{21}x_3^2 \\
&\quad - 0.22919\kappa_{22}x_3^2 + 1.633\times10^{-17}\kappa_{11}x_3 + 1.633\times10^{-17}\kappa_{22}x_3 \\
&\quad - 0.46668x_3\epsilon_{11} - 0.45839x_3\epsilon_{22} + 3.225\times10^{-18}\epsilon_{11} + 3.198\times10^{-18}\epsilon_{22} \\
w_1^{L6} &= \gamma_{13}\left(-1.268\times10^{1}x_3^3 + 4.638\times10^{-3}x_3^2 + 5.924\times10^{-1}x_3 + 4.335\times10^{-2}\right) \\
&\quad + \gamma_{23}\left(1.7322\times10^{-1}x_3^3 - 1.5116\times10^{-2}x_3^2 + 2.2918\times10^{-1}x_3 + 4.1382\times10^{-2}\right) \\
w_2^{L6} &= \gamma_{13}\left(-6.4884\times10^{1}x_3^3 + 1.6305\times10^{-2}x_3^2 + 2.6183\times10^{-1}x_3 + 4.6709\times10^{-2}\right) \\
&\quad + \gamma_{23}\left(2.4745\times10^{-2}x_3^3 - 4.6414\times10^{-3}x_3^2 + 3.9392\times10^{-1}x_3 - 4.3946\times10^{-2}\right) \\
w_3^{L6} &= 0.01921\kappa_{11} - 6.4816\times10^{-5}\kappa_{12} - 6.4816\times10^{-5}\kappa_{21} + 0.01934\kappa_{22} \\
&\quad + \gamma_{12}\left(1.276\times10^{-19}x_3^2 + 2.0741\times10^{-3}x_3 + 2.5926\times10^{-4}\right) \\
&\quad + \gamma_{21}\left(1.276\times10^{-19}x_3^2 + 2.0741\times10^{-3}x_3 + 2.5926\times10^{-4}\right) \\
&\quad - 0.23127\kappa_{11}x_3^2 + 2.0741\times10^{-3}\kappa_{12}x_3^2 + 2.0741\times10^{-3}\kappa_{21}x_3^2 \\
&\quad - 0.23127\kappa_{22}x_3^2 + 4.8997\times10^{-17}\kappa_{11}x_3 + 5.1038\times10^{-19}\kappa_{12}x_3 \\
&\quad - 4.6254\times10^{-1}x_3\epsilon_{11} - 4.6254\times10^{-1}x_3\epsilon_{22} + 5.1853\times10^{-4}\epsilon_{11} - 5.1853\times10^{-4}\epsilon_{22} \\
w_1^{L7} &= \gamma_{13}\left(-3.978\times10^{0}x_3^3 + 2.694\times10^{-3}x_3^2 + 9.808\times10^{-1}x_3 + 1.325\times10^{-1}\right) \\
&\quad + \gamma_{23}\left(1.980\times10^{-1}x_3^3 - 1.686\times10^{-2}x_3^2 - 1.316\times10^{-1}x_3 - 4.115\times10^{-2}\right) \\
w_2^{L7} &= \gamma_{13}\left(-5.519\times10^{1}x_3^3 + 1.369\times10^{-2}x_3^2 - 9.492\times10^{-2}x_3 - 3.486\times10^{-2}\right) \\
&\quad + \gamma_{23}\left(-2.172\times10^{-3}x_3^2 + 6.603\times10^{-2}x_3 - 1.193\times10^{-1}\right) \\
w_3^{L7} &= 0.01908\kappa_{11} + 6.482\times10^{-5}\kappa_{12} + 6.482\times10^{-5}\kappa_{21} + 0.01947\kappa_{22} \\
&\quad + \gamma_{12}\left(1.276\times10^{-19}x_3^2 + 1.276\times10^{-19}x_3 - 2.593\times10^{-4}\right) \\
&\quad + \gamma_{21}\left(1.276\times10^{-19}x_3^2 + 1.276\times10^{-19}x_3 - 2.593\times10^{-4}\right) \\
&\quad - 0.22919\kappa_{11}x_3^2 - 5.104\times10^{-19}\kappa_{12}x_3^2 - 5.104\times10^{-19}\kappa_{21}x_3^2 - 0.23334\kappa_{22}x_3^2 \\
&\quad - 1.633\times10^{-17}\kappa_{11}x_3 - 5.104\times10^{-19}\kappa_{12}x_3 - 5.104\times10^{-19}\kappa_{21}x_3 \\
&\quad - 4.584\times10^{-1}x_3\epsilon_{11} - 4.667\times10^{-1}x_3\epsilon_{22} + 1.556\times10^{-3}\epsilon_{11} - 1.556\times10^{-3}\epsilon_{22}
\end{aligned}
$$

} Plate's warping functions

Box IV.

$$
\left.
\begin{aligned}
w_1^{L8} &= \gamma_{13}\left(3.920\times10^{0}x_3^3 + 5.1107\times10^{-4}x_3^2 + 6.0314\times10^{-1}x_3 + 1.7971\times10^{-2}\right)\\
&\quad + \gamma_{23}\left(1.7197\times10^{-1}x_3^3 - 1.4358\times10^{-2}x_3^2 - 4.1917\times10^{-1}x_3 - 1.3131\times10^{-1}\right)\\
w_2^{L8} &= \gamma_{13}\left(-6.3525\times10^{1}x_3^3 + 1.5584\times10^{-2}x_3^2 - 3.7756\times10^{-1}x_3 - 1.1917\times10^{-1}\right)\\
&\quad + \gamma_{23}\left(-1.9843\times10^{-2}x_3^3 - 8.2541\times10^{-4}x_3^2 + 4.0458\times10^{-1}x_3 - 1.6541\times10^{-2}\right)\\
w_3^{L8} &= 0.01937\kappa_{11} + 3.5649\times10^{-4}\kappa_{12} + 3.5649\times10^{-4}\kappa_{21} + 0.01918\kappa_{22}\\
&\quad + \gamma_{12}\left(1.276\times10^{-19}x_3^2 - 2.0741\times10^{-3}x_3 - 1.0371\times10^{-3}\right)\\
&\quad + \gamma_{21}\left(1.276\times10^{-19}x_3^2 - 2.0741\times10^{-3}x_3 - 1.0371\times10^{-3}\right)\\
&\quad - 0.23127\kappa_{11}x_3^2 - 2.0741\times10^{-3}\kappa_{12}x_3^2 - 2.0741\times10^{-3}\kappa_{21}x_3^2 - 0.23127\kappa_{22}x_3^2\\
&\quad + 5.551\times10^{-17}\kappa_{11}x_3 - 4.337\times10^{-19}\kappa_{12}x_3 - 4.337\times10^{-19}\kappa_{21}x_3 + 4.900\times10^{-17}\kappa_{22}x_3\\
&\quad - 4.6254\times10^{-1}x_3\epsilon_{11} - 4.6254\times10^{-1}x_3\epsilon_{22} - 4.3802\times10^{-17}\epsilon_{11} - 3.9465\times10^{-17}\epsilon_{22}
\end{aligned}
\right\}\ \text{Plate's warping functions}
$$

Box V.

References

[1] Zimmermann R, Rolfes R. POSICOSS—improved post-buckling simulation for design of fibre composite stiffened fuselage structures. Compos Struct 2006;73(2):171–4.

[2] Mo Y, Ge D, Zhou J. Experiment and analysis of hat-stringer-stiffened composite curved panels under axial compression. Compos Struct 2015;123:150–60.

[3] Ahmadi H, Rahimi G. Analytical and experimental investigation of transverse loading on grid stiffened composite panels. Composites B 2019;159:184–98.

[4] Wu Q, Hu S, Tang X, Liu X, Chen Z, Xiong J. Compressive buckling and post-buckling behaviors of J-type composite stiffened panel before and after impact load. Compos Struct 2023;304:116339.

[5] Riccio A, Linde P, Raimondo A, Buompane A, Sellitto A. On the use of selective stitching in stiffened composite panels to prevent skin-stringer debonding. Composites B 2017;124:64–75.

[6] Suriani M, Rapi HZ, Ilyas R, Petru M, Sapuan S. Delamination and manufacturing defects in natural fiber-reinforced hybrid composite: A review. Polymers 2021;13(8):1323.

[7] Kong X, Yang Y, Gan J, Yuan T, Ao L, Wu W. Experimental and numerical investigation on the detailed buckling process of similar stiffened panels subjected to in-plane compressive load. Thin-Walled Struct 2020;148:106620.

[8] Akterskaia M, Jansen E, Hühne S, Rolfes R. Efficient progressive failure analysis of multi-stringer stiffened composite panels through a two-way loose coupling global-local approach. Compos Struct 2018;183:137–45.

[9] Kolanu NR, Raju G, Ramji M. Experimental and numerical studies on the buckling and post-buckling behavior of single blade-stiffened CFRP panels. Compos Struct 2018;196:135–54.

[10] Zhou W, Shi Z, Rong Q, Bai X, Zeng Y, Lin J. Experimental and numerical investigations on buckling behaviour of stiffened panel during creep age forming. Thin-Walled Struct 2022;172:108940.

[11] Mallela UK, Upadhyay A. Buckling of laminated composite stiffened panels subjected to in-plane shear: A parametric study. Thin-Walled Struct 2006;44(3):354–61.

[12] Boni L, Fanteria D, Lanciotti A. Post-buckling behaviour of flat stiffened composite panels: Experiments vs. analysis. Compos Struct 2012;94(12):3421–33.

[13] van Dooren KS, Tijs B, Waleson J, Bisagni C. Skin-stringer separation in post-buckling of butt-joint stiffened thermoplastic composite panels. Compos Struct 2023;304:116294.

[14] Castro SG, Mittelstedt C, Monteiro FA, Arbelo MA, Degenhardt R, Ziegmann G. A semi-analytical approach for linear and non-linear analysis of unstiffened laminated composite cylinders and cones under axial, torsion and pressure loads. Thin-Walled Struct 2015;90:61–73.

[15] Buermann P, Rolfes R, Tessmer J, Schagerl M. A semi-analytical model for local post-buckling analysis of stringer-and frame-stiffened cylindrical panels. Thin-Walled Struct 2006;44(1):102–14.

[16] Zhou W, Li Y, Shi Z, Lin J. An analytical solution for elastic buckling analysis of stiffened panel subjected to pure bending. Int J Mech Sci 2019;161:105024.

[17] Huang S, Qiao P. A novel semi-analytical method for buckling analysis of stiffened laminated composite plates. Thin-Walled Struct 2020;148:106575.

[18] Padhee SS. A synergetic micromechanics model for fiber reinforced composites [Ph.D. thesis], 2014.

[19] Kamineni JN, Burela RG. Constraint method for laminated composite flat stiffened panel analysis using variational asymptotic method (VAM). Thin-Walled Struct 2019;145:106374.

[20] O'Leary JR, Harari I. Finite element analysis of stiffened plates. Comput Struct 1985;21(5):973–85.

[21] Riccio A, Raimondo A, Scaramuzzino F. A robust numerical approach for the simulation of skin-stringer debonding growth in stiffened composite panels under compression. Composites B 2015;71:131–42.

[22] Kolanu NR, Raju G, Ramji M. A unified numerical approach for the simulation of intra and inter laminar damage evolution in stiffened CFRP panels under compression. Composites B 2020;190:107931.

[23] Aydin Komur M, Sen F, Ataş A, Arslan N. Buckling analysis of laminated composite plates with an elliptical/circular cutout using FEM. Adv Eng Softw 2010;41(2):161–4.

[24] Shojaee S, Valizadeh N, Izadpanah E, Bui T, Vu T-V. Free vibration and buckling analysis of laminated composite plates using the NURBS-based isogeometric finite element method. Compos Struct 2012;94(5):1677–93.

[25] Akterskaia M, Jansen E, Hallett SR, Weaver P, Rolfes R. Analysis of skin-stringer debonding in composite panels through a two-way global-local method. Compos Struct 2018;202:1280–94.

[26] Perret A, Mistou S, Fazzini M, Brault R. Global behaviour of a composite stiffened panel in buckling. Part 2: Experimental investigation. Compos Struct 2012;94(2):376–85.

[27] Zhu S, Yan J, Chen Z, Tong M, Wang Y. Effect of the stiffener stiffness on the buckling and post-buckling behavior of stiffened composite panels - Experimental investigation. Compos Struct 2015;120:334–45.

[28] Ahmadi H, Rahimi G. Analytical and experimental investigation of transverse loading on grid stiffened composite panels. Composites B 2019;159:184–98.

[29] Shahgholian-Ghahfarokhi D, Rahimi G, Liaghat G, Degenhardt R, Franzoni F. Buckling prediction of composite lattice sandwich cylinders (CLSC) through the vibration correlation technique (VCT): Numerical assessment with experimental and analytical verification. Composites B 2020;199:108252.

[30] Wilckens D, Odermann F, Kling A, Degenhardt R. Buckling and post buckling investigation of stringer stiffened CFRP panels under in-plane loading-experimental investigations. Adapt, Tolerant Effic Compos Struct 2012;189–97.

[31] Bisagni C, Vescovini R, Dávila CG. Single-stringer compression specimen for the assessment of damage tolerance of post-buckled structures. J Aircr 2011;48(2):495–502.

[32] Banat D, Mania R. Failure assessment of thin-walled FML profiles during buckling and postbuckling response. Composites B 2017;112:278–89.

[33] Khakimova R, Castro SG, Wilckens D, Rohwer K, Degenhardt R. Buckling of axially compressed CFRP cylinders with and without additional lateral load: Experimental and numerical investigation. Thin-Walled Struct 2017;119:178–89.

[34] Burela R, Bhadoria S, Harusampath D. Non-linear analysis of orthotropic hyperelastic plate using VAM. In: IOP conference series: materials science and engineering, vol. 1248, IOP Publishing; 2022, 012006.

[35] Phanendra Kumar A, Khajamoinuddin SM, Burela RG, Mahesh V, Harursampath D. Snap-through analysis of multistable laminate using the variational asymptotic method. Mech Based Des Struct Mach 2022;1–26.

[36] Kamineni JN, Burela RG. Constraint method for laminated composite flat stiffened panel analysis using variational asymptotic method (VAM). Thin-Walled Struct 2019;145:106374.

[37] Burela RG, Harursampath D. VAM applied to dimensional reduction of non-linear hyperelastic plates. Internat J Engrg Sci 2012;59:90–102, The Special Issue in honour of Victor L. Berdichevsky.

[38] Yu W, Tang T. Variational asymptotic method for unit cell homogenization of periodically heterogeneous materials. Int J Solids Struct 2007;44(11):3738–55.

[39] Harursampath D, Harish AB, Hodges DH. Model reduction in thin-walled open-section composite beams using variational asymptotic method. Part I: Theory. Thin-Walled Struct 2017;117:356–66.

[40] Peereswara Rao M, Harursampath D, Renji K. Prediction of inter-laminar stresses in composite honeycomb sandwich panels under mechanical loading using variational asymptotic method. Compos Struct 2012;94(8):2523–37.

[41] Hodges DH, Atilgan AR, Danielson DA. A geometrically non-linear theory of elastic plates. J Appl Mech 1993;60(1):109–16.
[42] Reissner E. On transverse bending of plates, including the effect of transverse shear deformation. Int J Solids Struct 1975;11(5):569–73.
[43] Paz J, Raimondo A, Bisagni C. Experimental study of post-buckled single-stringer composite specimens under fatigue loads with different load levels and load ratios. Composites B 2023;255:110606.
[44] Raimondo A, Urcelay Oca I, Bisagni C. Influence of interface ply orientation on delamination growth in composite laminates. J Compos Mater 2021;55(27):3955–72.
[45] Krueger R. A summary of benchmark examples to assess the performance of quasi-static delamination propagation prediction capabilities in finite element codes. J Compos Mater 2015;49(26):3297–316.